UNIVERSIDAD AUTÓNOMA DE BAJA CALIFORNIA

POSGRADO DE MAESTRÍA Y DOCTORADO EN CIENCIAS QUÍMICAS E INGENIERÍA

FACULTAD DE CIENCIAS QUÍMICAS E INGENIERÍA

¨Membranas antibacterianas activadas por luz para la reparación de hernias¨

TESIS

Para obtener el título de **Maestra en Ciencias** por

VANESSA GONZALEZ GUERRERO

Supervisores

Dr. Héctor Alfonso Magaña Badilla

Dra. Kenia Palomino Vizcaíno

Tijuana, Baja California

Diciembre, 2024

LIGHT ACTIVATED ANTIBACTERIAL MEMBRANES FOR HERNIA REPAIR

By

VANESSA GONZALEZ GUERRERO

A thesis submitted as part of the requirements for
the degree of ResM in Science and Engineering
(International) at the School of Engineering and
Materials Science, Queen Mary University of
London, London, UK

Supervisors:
Prof. Kathleen Elizabeth Tanner
Prof. Ana Jorge Sobrido

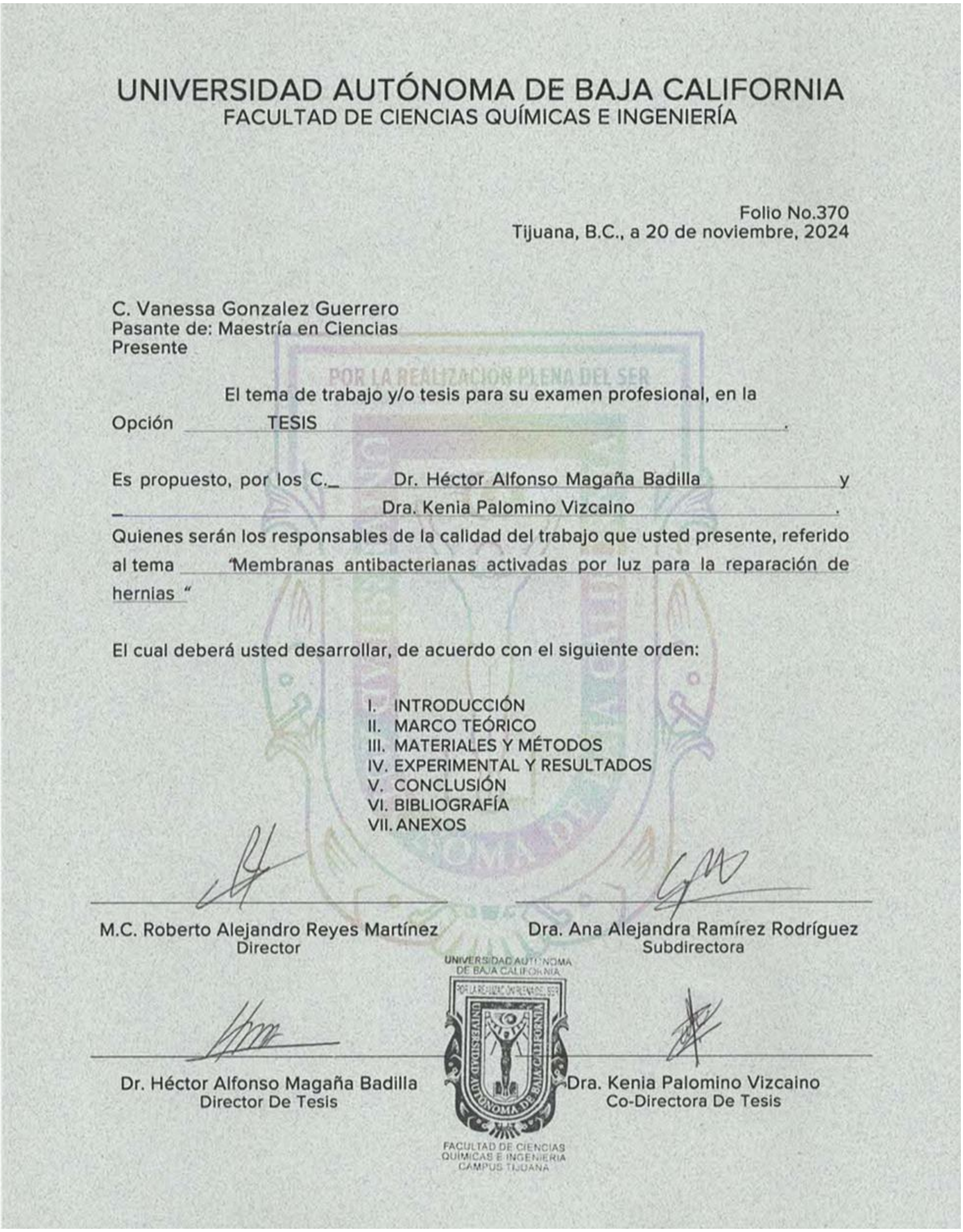

UNIVERSIDAD AUTÓNOMA DE BAJA CALIFORNIA
FACULTAD DE CIENCIAS QUÍMICAS E INGENIERÍA

Folio No.370
Tijuana, B.C., a 20 de noviembre, 2024

C. Vanessa Gonzalez Guerrero
Pasante de: Maestría en Ciencias
Presente

El tema de trabajo y/o tesis para su examen profesional, en la

Opción TESIS.

Es propuesto, por los C. Dr. Héctor Alfonso Magaña Badilla y Dra. Kenia Palomino Vizcaino.

Quienes serán los responsables de la calidad del trabajo que usted presente, referido al tema "Membranas antibacterianas activadas por luz para la reparación de hernias"

El cual deberá usted desarrollar, de acuerdo con el siguiente orden:

- I. INTRODUCCIÓN
- II. MARCO TEÓRICO
- III. MATERIALES Y MÉTODOS
- IV. EXPERIMENTAL Y RESULTADOS
- V. CONCLUSIÓN
- VI. BIBLIOGRAFÍA
- VII. ANEXOS

M.C. Roberto Alejandro Reyes Martínez
Director

Dra. Ana Alejandra Ramírez Rodríguez
Subdirectora

Dr. Héctor Alfonso Magaña Badilla
Director De Tesis

Dra. Kenia Palomino Vizcaino
Co-Directora De Tesis

DECLARACIÓN DE ORIGINALIDAD Y COLABORACIÓN ENTRE UNIVERSIDADES

Yo, Vanessa Gonzalez Guerrero, confirmo por la presente que la investigación presentada en esta tesis es obra mía. En los casos en los que se ha contado con la colaboración o el apoyo de otras personas, se hace constar a continuación el reconocimiento correspondiente y se indican claramente mis contribuciones específicas. También se menciona cualquier material publicado anteriormente. Afirmo que he tomado las debidas precauciones para garantizar la originalidad de este trabajo y que, según mi leal saber y entender, no infringe ninguna ley del México ni Reino Unido, ni vulnera derechos de autor o de propiedad intelectual de terceros, ni contiene información confidencial. Esta investigación fue generada dentro de un programa dual entre **Universidad Autónoma de Baja California** (UABC) y **Queen Mary University of London** (QMUL), bajo el **convenio** "**2486-CONV0556601-2397**", donde se generó una colaboración académica entre ambas instituciones académicas para la realización de esta tesis, la cual consiste en un año de estudio en la UABC, México y el segundo año se cursó en QMUL, Inglaterra, Reino Unido. El responsable académico de la estudiante en UABC, es el Dr. Héctor Alfonso Magaña Badilla; por parte de QMUL es la Dra. Kathleen Elizabeth Tanner (responsable de este proyecto de investigación). Entiendo que las Universidades se reservan el derecho de utilizar software de detección de plagio para revisar la versión electrónica de esta tesis. Los derechos de autor de esta tesis pertenecen al autor, y ninguna parte de esta puede ser citada o utilizada sin mi consentimiento previo por escrito.

Firma: Vanessa Gonzalez Guerrero

Fecha: 3/Diciembre/2024.

STATEMENT OF ORIGINALITY

I, Vanessa Gonzalez Guerrero, hereby confirm that the research presented in this thesis is my own work. Where collaborative efforts or support from others have been involved, appropriate acknowledgment is given below, and my specific contributions are clearly indicated. Any previously published material has also been acknowledged. I affirm that I have taken due care to ensure the originality of this work, and to the best of my knowledge, it does not violate any UK laws, infringe upon third-party copyrights or Intellectual Property Rights, nor contain confidential information.

I understand that the University reserves the right to use plagiarism detection software to review the electronic version of this thesis.

I also confirm that this thesis has not been submitted for a degree at this or any other institution. The copyright of this thesis belongs to the author, and no part of it may be quoted or used without my prior written consent.

Signature: Vanessa Gonzalez Guerrero

Date: 26/09/23

ABSTRACT

This thesis investigates the production of a mesh synthesised from a novel biocompatible, resorbable, and biodegradable polymer, polyhydroxybutyrate (PHB), using electrospinning. PHB is known for its biocompatibility, degradability and biomechanical properties, which make it suitable for surgical hernia repair, tissue regeneration, and bone tissue repair. To enhance the mesh, citric acid and 1,5-diaminonaphthalene (1,5-DAN)-synthesised carbon nanodots (CNDs) was incorporated at concentrations of 1%, 2.5%, 5%, and 10% w/v.

The CNDs impart antimicrobial properties, as they can release singlet oxygen species (a reactive oxygen species that kills bacteria) when activated by UV or visible light on command. Coaxial electrospinning was chosen for this process, with non-filled PHB as the core solution and CNDs added to the PHB in the outer shell. Since CNDs are polar and cannot be directly added, a PHB/CND solution was created, reducing PHB concentration to 5% to facilitate the process.

Additionally, single-needle electrospinning of plain PHB (without CNDs) was performed to compare the morphological, thermal properties, and cytocompatibility of the meshes. CNDs were characterised for their optical properties using fluorescence and UV-Vis spectroscopy to ensure visible light activation, which is more practical for hernia repair. XPS analysis was used to determine nitrogen content and distribution in the meshes across the varying CND concentrations. Additionally, an MTT Assay was performed comparing different conditions to which the fibres were subjected, to determine if the CNDs loaded fibre meshes were biocompatible and could show potential as an implant to treat hernias.

Resulting from this research, a biodegradable mesh was created from PHB fibres. These fibres were loaded with carbon nanodots, which exhibit fluorescent behaviour when activated by visible light. This property suggests their potential application in hernia repair.

Keywords: coaxial electrospinning, core-shell electrospinning, single needle electrospinning, carbon nanodots, polyhydroxybutyrate, hernia repair.

ACKNOWLEDGMENTS

I thank God for giving me the opportunity to do this dual master's program.

Thank you to the School of Engineering and Materials Science in Queen Mary, University of London; to the Faculty of Chemical Sciences and Engineering in the Autonomous University of Baja California studentship and the CONAHCYT scholarship for funding my research.

I would like to extend my heartfelt gratitude to my primary supervisors, Professor Elizabeth Tanner and Dr. Hector Alfonso Magaña Badilla. It has truly been a privilege to work under their guidance. Their unwavering support and insightful advice have been fundamental in shaping my work and my personal growth throughout this journey. I deeply appreciate the time and effort they dedicated to mentoring me, which has made a significant impact on my experience.

I would like to express my sincere appreciation to my secondary supervisors, Prof. Ana Jorge Sobrido, Dr. Kenia Palomino Vizcaino and Dr. Giovanni Palomino Vizcaino. I am infinitely grateful for their kind words of encouragement and shared knowledge. Thank you for allowing me to be part of your work team, for opening the doors of your laboratory. For accepting me as a person, always trusting me as a student and a professional.

I am also grateful to all my lab group friends who have made this experience so gleeful, even while working. I would like to give my special thanks to Hattie Chisnall and Michael Thielke who kindly helped me analyse my XPS data and graphs. Warm thanks to Gabriela Valenzuela, Jesus Vazquez, Mauricio Murillo, Maadri Pathiranage, Yi Wang, and Carlos Mingoes.

I would like to thank all the SEMS technicians who kindly had the time to instruct me to use their equipment, trusted me and, not less importantly, shared their vast techniques and knowledge with me. Special thanks to Subash Rai and Qasim Zia from the NanoVision Facility, Richard Whiteley from the X-ray Diffraction Facility at QMUL who, additionally, considerately processed all my XRD samples.

My special thanks to my amazing parents and sister from the bottom of my heart, for everything they have given me. Thank you for your support throughout my life because without you I would not be who I am and this work would not be possible without your guidance and trust.

To my family, for believing in me, trusting that I could do this even when I doubted.

To my exceptional friends who are home back in Mexico and, to the friends that I made along the way. Thank you for always being there for me whenever I needed you.

LIST OF ABBREVIATIONS

μg	Microgram
μl	Microlitre
ºC	Degrees Celsius
2D	Two-dimensional
3D	Three-dimensional
APDI/aPDI	Antibacterial Photodynamic Inactivation
ATR-FTIR	Attenuated Total Reflectance Fourier Transform Infrared Spectroscopy
Chl	Chloroform
CND/CNDs, C-dots	Carbon nanodots
Contact Angle, θ (theta), DSA	Contact Angle Measurement of Sessile Drops, Drop Shape Analysis
DLS	Dynamic Light Scattering
DSC	Differential Scanning Calorimetry
EDXS/EDS	Energy-dispersive X-ray Spectroscopy often shortened to Energy Dispersive Spectroscopy (EDS).
ECM	Extracellular Matrix
FBS	Foetal bovine serum
g/mol	Grams per mol
H_2O	Water
ID	Internal diameter
kV	Kilovolts
M	Mol
m/v	Mass/volume ratio
MD	Medical device
mL	Mililitres
mm	Milimitres
Mn	Number average molecular weight
Mw	Molecular weight
nm	Nanometre
NP/NPs	Nanoparticles

NT/NTs	Nanotube
$^1O_2$	Singlet oxygen
P/S	Penicillin/streptomycin
PAN	Polyacrylonitrile
PBS	Phosphate Buffered Saline
PCL	Polycaprolactone
PDI	Polydispersity index
PLA	Poly(lactic acid), Polylactide
PGA	Polyglycolide
PH	Primary hernia
PHA	Polyhydroxyalkanoates
PHB	Poly[(*R*)-3-hydroxybutyric acid], Poly(3-hydroxybutyrate), Polyhydroxybutyrate
PS	Photosensitiser
QDs, Q-dots	Quantum dots
R-3-HB	R-3-hydroxybutyrate
ROS	Reactive oxygen species
rpm	Rotations per minute
SEM	Scanning Electron Microscopy
SH	Secondary hernia
SSI	Surgical Site Infection
TEM	Transmission Electron Microscopy
Tg	Glass transition temperature
TGA	Thermogravimetric analysis
UV	Ultraviolet
UV-Vis Spectroscopy	Ultraviolet-Visible Spectroscopy
% v/v	Volume per volume
wt%	Weight percent
w/v	Weight per volume
XPS	X-ray Photoelectron Spectroscopy
XRD	X-Ray Diffraction

Contents

List of Figures

List of Tables

Chapter 1

Introduction

1.1 Background

A hernia occurs when an internal organ or tissue pushes through a weakened area in the surrounding muscle or connective tissue. This condition commonly affects areas such as the abdomen, groin, or diaphragm, leading to discomfort, pain, and potential complications such as strangulation of the protruding tissue. A range of medical conditions, such as trauma, diseases that weaken the abdominal wall or surgery can cause them. Hernias do not heal on their own, and surgical intervention is often necessary to repair the defect and prevent further harm [3], [4], [5].

Throughout history, hernias have been a condition that greatly affected the population, with inguinal hernias being particularly concerning due to their higher incidence. Despite the relatively slow progression of the disease, it eventually grows to a size that significantly hinders the patient's ability to carry out daily activities. This is why, even in ancient times, both surgeons and physicians sought solutions to address this distressing condition [3].

The ancient Egyptians, initially treated hernias by using bandages as external support. Over time, this approach evolved into the use of custom-made hernia belts designed to keep the hernia sac inside the body cavity. The first attempts at suturing techniques emerged in the 16th century, led by Italian anatomist Gabrielle Falloppio, who proposed using gold stitches for incisions. Gold was valued for its bioinert non-corroding properties, a tradition dating back to ancient Greece. Over the years, other metals were introduced for sutures, including lead (by the physician Physik in 1816), silver (such as Mettauer in 1822 and Bassini in 1887), and even an inert metal such as tantalum (such as by the physician Burke in 1940). However, the disadvantage of surgical interventions in the case of inguinal hernias, was the possibility of sepsis and that to remove completely the hernia, the incision was performed for castration, or to either cut and tie off the hernial sac or encircle the spermatic cord [3], [4].

Nevertheless, the emergence of hernia meshes have significantly transformed the field of hernia surgery [5]. Hernia meshes are medical devices made from synthetic or biological materials, designed to reinforce the weakened tissue and reduce the likelihood of recurrence. By providing structural support to the repaired area, these meshes distribute tension more evenly, allowing for a more durable repair compared to traditional suturing methods alone.

The use of mesh-based repair has become the standard of care in modern hernia surgery, particularly for larger or more complex hernias. It offers numerous advantages, including reduced recovery time compared to surgical sutures, lower recurrence rates, provides additional support to the weakened tissue and there are minimal invasive options to allocate the hernia such as laparoscopically [6], [7]. Despite these benefits, discussion remains around potential risks associated with hernia meshes, such as infection, adhesion, or mesh migration, which have prompted ongoing innovation in mesh design and materials.

Recent advances in hernia mesh technology focus on biocompatible and biodegradable materials that degrade over time, eliminating long-term foreign body complications. Hybrid meshes combine synthetic durability with biological materials that promote natural tissue integration, reducing the risk of rejection. Some meshes also feature drug delivery systems, releasing anti-inflammatory or pain-relieving agents directly at the surgical site to aid healing and prevent infection. Additionally, nanotechnology-enhanced meshes incorporate antimicrobial coatings and tissue regeneration agents, further promoting natural tissue repair and reducing complications. These innovations aim to improve safety, healing, and overall outcomes [7].

1.1.1 *Aims*

Hernia repair is essential to prevent severe complications, such as strangulation in inguinal hernias, which can result from untreated hernias. While advances in surgical methods, including laparoscopic and tension-free mesh repairs, have significantly improved outcomes, post-operative infections remain a persistent challenge, compromising recovery and patient safety. For this reason, it was decided to develop an enhanced electrospun mesh made from a natural and biodegradable polymer, polyhydroxybutyrate. This mesh would be integrated with light-activated carbon nanodots that when triggered could kill bacteria on instruction, reducing the risk of infection and further advancing the safety and effectiveness of hernia repair procedures.

1.1.2 *Objectives*

I. Use electrospinning to develop a mesh from a natural origin polymer polyhydroxybutyrate (PHB).

II. Enhance the mesh by adding light-activated carbon nanodots (CNDs) made from citric acid and 1,5-diaminonaphtalene (1,5-DAN) to provide a prophylaxis and antibacterial application.

III. Evaluate the addition of CNDs in concentrations of 0% (without the addition of CNDs, as a control), 1%, 2.5%, 5% and 10%, being 2.5% the concentration reported in literature to be biocompatible and effective against *S. aureus* (98.3%), *E. coli* (99.99+%), *P. aeruginosa* (99.99+%) and *B. subtilis* (99.99+%) [8].

IV. Generate fibre meshes with the addition of CNDs, via single needle electrospinning (without CNDs, 0%) and using coaxial electrospinning (1%, 2.5%, 5% and 10%).

V. Observe the morphology of the CNDs and coaxial fibres using electron microscopy and compare the morphology differences between fibres of different concentrations as well as calculate the fibre diameter using SEM Microscopy.

VI. Characterise the synthesised CNDs through UV-Vis and Fluorescence Spectroscopy and DLS size measurement.

VII. Characterise the produced meshes and CNDs via ATR-FTIR Spectroscopy, thermal techniques such as TGA and DSC, Contact Angle measurement and XPS Analysis.

VIII. Evaluate the cytocompatibility of the different fibre meshes using a MTT Assay.

Chapter 2

Literature Review

2.1 An Introduction to Hernias

A hernia can be defined as a condition where there is an abnormal protrusion of an organ or tissue through a weakened area in the surrounding muscle or connective tissue, usually occurring in the abdominal wall. This condition often results in a visible lump and can cause pain or complications if left untreated. The hernia needs to be treated as urgently since this condition only increases over time (*Figure 2.1.1*). Hernia repair is among the most commonly performed surgical procedures globally.

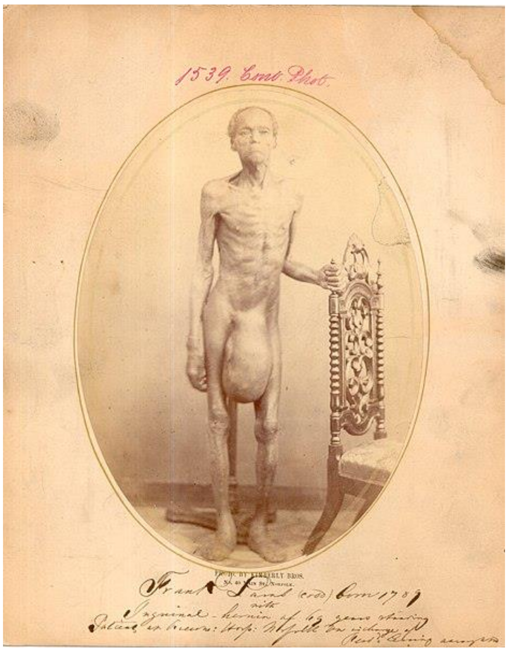

Figure 2.1.1: Frank Lamb, a 69-year-old man, has a long history of left inguinal hernia, dating back to when he was just 9 years old while living as a slave in North Carolina. Information is sourced from the Otis Historical Archives of the National Museum of Health and Medicine (Komorowski *et al*, 2014) [3].

2.1.1 *Types of Hernias*

As previously mentioned, hernias are mostly located in the abdominal wall *(Figure 2.1.2)*, but they can also be allocated upper thigh, chest cavity, lumbar region and in the pelvic region.

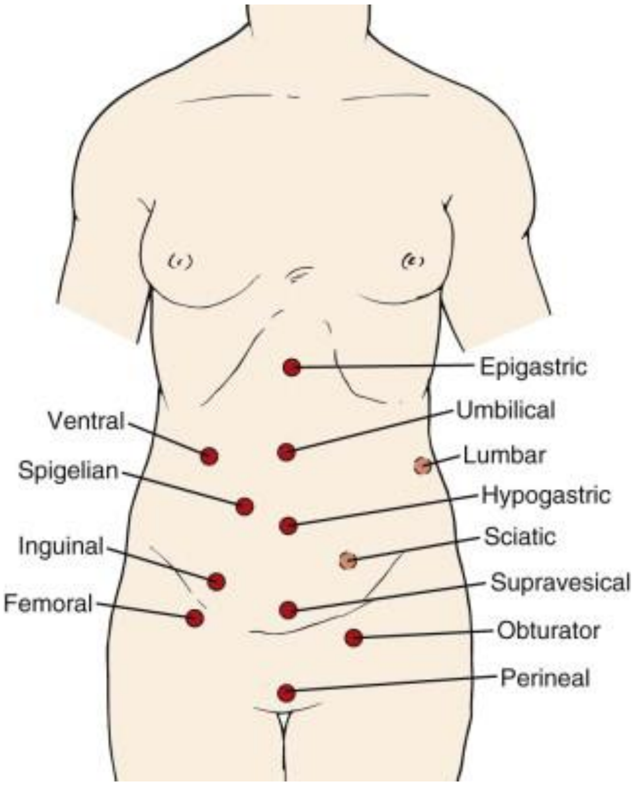

Figure 2.1.2: Anatomical representation of the location of the most common hernias [9].

Table 2.1.1 provides an overview of the most frequently encountered types of hernias shown in *Figure 2.1.2*, including their anatomical locations, prevalence in men and women, incidence rates in the general population, and key characteristics [6]. These hernias represent the majority of cases seen in clinical practice and often vary based on factors such as age, gender, and lifestyle. Understanding the distinctions between these common hernia types is crucial for accurate diagnosis and effective treatment.

Table 2.1.1: Most frequently occurring hernias [10].

Types of hernias	Anatomical location	Frequency	Characteristics	Relevant age groups	Reference
Ventral	Anterior abdominal wall	Approximately 10-15% of all abdominal hernias More common in men	Encompassing term used to describe hernias that develop through the front of the abdominal wall, such as, umbilical and incisional hernias	Occur in all age groups, but primarily in adults over 50	[11], [12]
Spigelian	Along the Spigelian fascia	Incidence of 0.1-2% of all hernias, being more common in women	Often asymptomatic initially	Common in adults between 40-70 years old	[13]
Inguinal	Groin area Direct or indirect	90% of cases are men Represent 70-70-755% of all hernias	Indirect hernias are congenital; therefore, they can affect children Direct are acquired	Common in infants and adults over 40	[14], [15]
Femoral	Femoral canal	More common in women (70%) Represents 3-5% of all hernias	Presents as a bulge in the upper thigh, associated with a higher risk of strangulation than inguinal hernias	Typically seen in adults above 60 years old	[16], [17]
Epigastric	Epigastric region	Represents 1-5% of abdominal hernias Affects both males and females	Frequently associated with increased intra-abdominal pressure due to obesity, pregnancy, or heavy lifting	Common in adults between 20-60 years old	[6], [12]
Umbilical	Umbilicus	In adults is 6-14% of all hernias In children, up to 10-30% of all newborns	In adults is acquired, often post-pregnancy. Congenital in infants	Common in infants and women	[12], [18]
Lumbar	Lumbar region	Less than 2% of abdominal hernias, can affect both men and women	Can be congenital but is often acquired by trauma or surgery	More common in adults over 40	[1], [10]
Hypo-gastric	Hypogastric region	Very rare	Often confused with other abdominal wall hernias	Mostly seen in adults	[12]

Sciatic	Sciatic Notch in the pelvic cavity	Extremely rare Less than 1% of all hernias	Can cause sciatic pain or discomfort	Mostly in elderly population	[19]
Supra-vesical	Above the bladder Pelvic cavity	Rare, constituting less than 1% of all hernias More common in men	May present with urinary symptoms or discomfort	Generally seen in elderly population	[20]
Obturator	Obturator foramen in the pelvic bone	Extremely rare Less than 1% of all hernias	Presents nonspecific symptoms, such as abdominal pain or intestinal obstruction	Predominantly women over 70 years	[21]
Perineal	Perineal region through the pelvic floor	Rare, represents less than 1% of pelvic surgeries Occur in both men and women	Caused by weakness or defect in the pelvic floor, specifically within the urogenital diaphragm Presents perineal protrusion and pain or discomfort	Occur mostly in elderly patients	[22]

These various hernia types highlight that even though abdominal hernias are the most frequently observed, hernias could be present in a range of unusual locations throughout, usually because of trauma or surgery, each with its own specific characteristics and implications for treatment.

Abdominal hernias can be classified as primary or secondary. Primary hernias (PH) or indirect hernias, develop in the anterior abdominal wall either due to a natural weakness or defect such as congenital hernias. Secondary hernias (SH) or direct hernias, occur through induced anatomical weakness, such as a previous surgical incision, pregnancy, obesity or age. Differences between these subtypes likely exist not only in size but also in clinical presentation and inherent characteristics. Most studies analysing the outcomes of hernia repairs have assessed PHs and SHs separately [25].

2.1.2 *Pathophysiology of Hernias*

To understand the pathophysiology of hernias, it is essential to recognise that they occur when the network of muscles does not provide the necessary mechanical strength and flexibility to support the internal organs inside the body cavity [23]. In case of the abdominal wall, the stability can be compromised by several factors; such as age, gender, anatomical variations, gestational defects that can assist in having congenital complications to generate certain types of hernias and, additionally, external factors such family history and environmental elements.

These elements include obesity, pregnancy, previous surgeries, smoking habits, ascites, between others [1]. Various molecular and cellular mechanisms have been proposed to explain the generation of hernias, but hernias are multifactorial, therefore, the biological underpinnings have not yet been understood. Hernias can be categorised as congenital or acquired [24].

The most studied congenital hernia is the inguinal type; therefore, the pathophysiology of this condition is the most studied amongst these type of hernias. Inguinal congenital hernias are associated with an open processus vaginalis, which is an invagination of the parietal peritoneum that forms prior to testicular descent through the inguinal canal during embryonic development [1]. Discussions suggest that all congenital and indirect inguinal hernias may result from a processus vaginalis that has never fully closed [25], [26]. In the case of inguinal hernias, there is double the number of indirect hernias than direct inguinal hernias.

For other congenital abdominal hernias, such as umbilical and epigastric, they appear as a protruding umbilicus. These hernias occur when after birth, the umbilical cord is no longer necessary, and the muscles usually tighten as the baby matures. However, when muscles are patent, a small opening is left and a loop of intestine or soft tissue, can penetrate the opening and cause the hernia [18], [27].

One area of focus to explain the aetiology of all hernias in a cellular mechanism discussed by different authors [28], is abnormal extracellular matrix (ECM) metabolism, particularly collagen metabolism, which has been linked to the development of hernias [24], [25]. In both primary and secondary hernias, there is not only a reduction in collagen but also an imbalance in the collagen types, collagen type I and collagen type III; in case studies, there are reports that mention that patients with inguinal hernias have a higher proportion of type III collagen compared to type I collagen. Type I collagen is known for having higher tensile strength than type III collagen [29], [30]. Additionally, factors such as growth factors, chronic inflammation, nutrition (increase in adipose tissue), and changes in cell types that attribute to pathological changes in the connective tissue have been suggested as contributing to hernia formation. Among the cellular participants, fibroblasts play a key role in maintaining ECM integrity and supporting the mechanical resilience of the abdominal wall [24].

2.1.3 *Challenges in Hernia Repair: Recurrence, Infection and Current Advances Aiming to Overcome these issues through Tissue Remodelling*

Hernia recurrence is a common complication following a reconstruction surgery, often attributed to the gradual weakening of the sutures or mesh over time. This weakening has been linked to disrupted collagen metabolism that prevents wound healing, driven by the underlying cellular pathology of the hernia. Activities such as lifting, bending, and coughing can exacerbate the condition [7].

Approximately 20 million inguinal hernia repairs are conducted globally each year. The estimated annual cost of hernia repairs is around $10 billion, a figure expected to grow as the aging population contributes to more recurrences; with men facing a 27% lifetime risk of developing an inguinal hernia, while women have a 3% risk [31]. It is reported that the number of hernia recurrences continues to rise annually, as current treatments often lead to poor recovery outcomes and various postoperative complications. Hence, when a hernia is diagnosed, patients are kept under review due to complications that often occur after general surgery, the most frequent being the opening or, delay in the closing, of the incision, chronic pain and surgical site infections. Different approaches have been made in this field, such as innovative surgical methods and various type of meshes, smart meshes being the most in demand [1], [7].

Depending on the size, severity and location of the hernia, different repair techniques and materials options are available. If the hernia is too severe, surgical intervention is required. Nevertheless, the use of hernia meshes is the preferred method as they are associated with less painful recovery, less invasive options and shorter hospitalisation periods compared to patients treated using sutures [7]. Additionally, sutures have benefited from technological advancements that have significantly decreased complications across various domains (*Table 2.1.2*) [32].

Table 2.1.2: Commonly used suture materials [32].

Surgical sutures	Types and characteristics
Natural absorbable	**Chitin**: Mild immune response; low tensile strength. **Catgut**: High degradation rate; significant antibody response. **Collagen**: Slight immune response; non-scaring.
Natural non-absorbable	**Cellulose**: High tensile strength; cheap material cost. **Silk**: Good biocompatibility; mild bacterial adhesion.
Synthetic absorbable	**Polyglycolic Acid (PGA):** Good biocompatibility; high tensile strength. **Poly(lactic-co-glycolic) acid**: High inflammation risk; water repellence.
Synthetic non-absorbable	**Polyamide (PA)**: Good elasticity; mild cell-mediated response. **Propylene (PP)**: High infection incidence; high tensile strength.
Metal	**Stainless Steel**: Tissue damage reports; poor manageability. **Nickel-Titanium**: High tensile strength; good biocompatibility.

Surgical suture materials have explored different areas such as the use of biodegradable and biocompatible materials, antiseptic biomaterials or coatings, high tensile strength components, the addition of biopharmaceutical agents that promote wound healing, anti-inflammatory drugs and growth factors [32]. Recent advancements in surgical sutures are contributing to improvements across various surgical specialties, beyond just hernia repair.

In parallel, one of the most common approaches to surgical repair, particularly for hernias, involves the use of mesh to close defects. Currently, there are three types of meshes available for hernia repair. They are categorized based on their origin into three types: synthetic, biological, and composite, the latter being a blend of both synthetic and biological materials [7], [33]. They can also be divided into prosthetic meshes and smart meshes or scaffolds. The difference between prosthetic and smart meshes can be found in that prosthetic meshes are often produced of synthetic materials and they are primarily designed to provide structural support for tissue repair; while smart meshes, often incorporate advanced technologies or materials that may include features such as drug delivery systems, sensors, or bioactive components that promote healing or monitor conditions (*Figure 2.1.3*) [1].

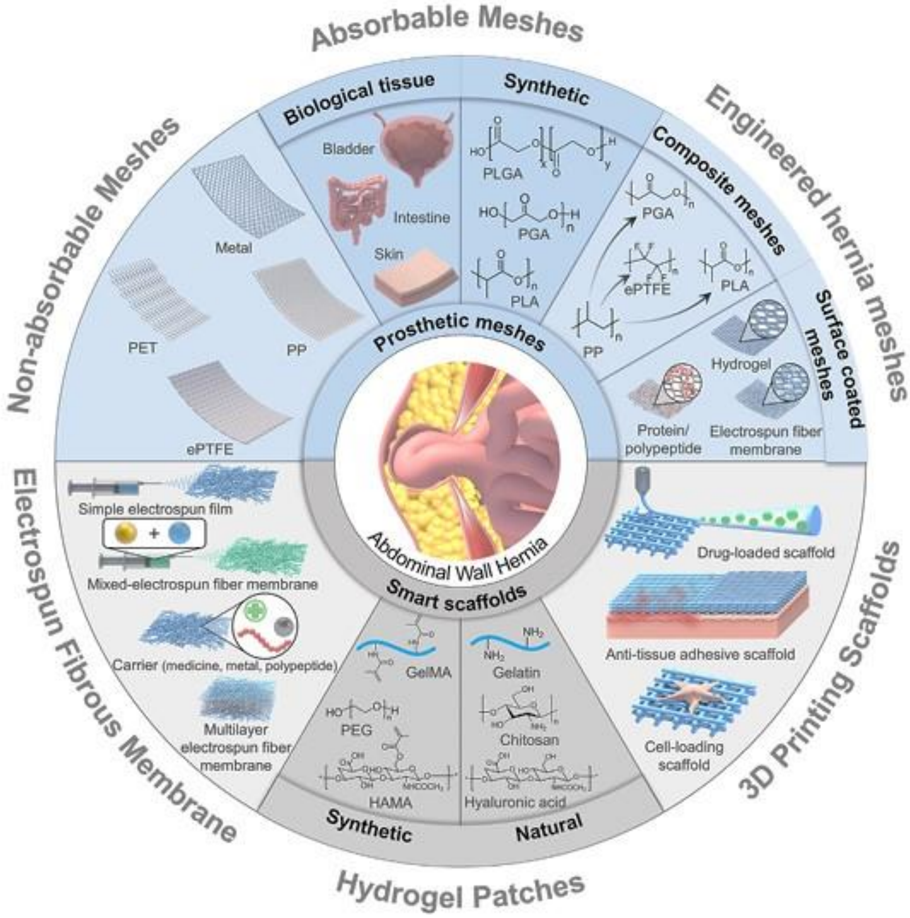

Figure 2.1.3: Abdominal wall hernia repair meshes, prosthetic and smart meshes. (Saiding *et al.*, 2023) Sourced from: [1]

Additionally, efforts have been made to continuously innovate and improve hernia meshes. Synthetic meshes are known to lower the hernia recurrence rate in ventral and inguinal hernia repair, however, they are prone to infection in both clean and contaminated repairs, which can necessitate further procedures to remove the infected mesh and address the larger hernia defect which is produced. Biological tissue based meshes have been proposed as an alternative to synthetic meshes to minimize infections.

It has been effectively used in contaminated cases to help prevent infections, thereby reducing post-operative complications and the need for further procedures, reducing mortality and morbidity due to infection caused by incarceration (the hernia becomes trapped in the abdominal wall or muscle and cannot be pushed back into place, the pressure generated where the hernia passes through the muscle wall cuts off the blood supply to the extruded tissue leading to necrosis of this extruded tissue) [36]. Moreover, the hybrid meshes, fabricated using a mixture of synthetic and biological components have been known to conserve the high tensile strength and preserve their substantial biocompatibility.

One of the most investigated strategies has been modifying commercial meshes using biocompatible agents like proteins, peptides, and engineered hydrogels to enhance the histocompatibility of hernia meshes. Electrospinning has emerged as a leading technique in tissue engineering for creating fibrous membranes with a high surface-area-to-volume ratio and ranging from nano-to micro-sized fibres. Due to their versatile composition, electrospun fibrous meshes have been explored in various applications, including wound dressings, biosensors and drug delivery systems. The technique's ability to achieve ideal mechanical strength in the fibres has made it a popular choice for abdominal wall hernia reconstruction in recent years. However, the inert nature of the raw materials used in electrospinning results in primarily hydrophobic fibres, which can hinder their histological integration during hernia repair. To achieve the necessary biocompatibility and mechanical strength for hernia repair, biodegradable polymers can be tailored by adjusting their concentration or incorporating more polar materials. This customization allows for the control of the resulting product's properties, enabling the development of specific features that are ideal for effective hernia repair [1], [37].

2.2 Electrospinning in Mesh Fabrication

2.2.1 *Introduction to Electrospinning Technology*

Electrospinning has advanced rapidly over the past few decades into a highly versatile technique for producing fibres with diameters ranging from micrometres to just a few nanometres [34]. This method enables the creation of fibres with unique morphologies for a vast number of applications across various fields. These include drug delivery, tissue engineering, new textiles fabrication, water and air filtration and sensor development [35].

Before the emergence of electrospinning, researchers used the electrospraying technique to disperse solutions and fine aerosols, harnessing electrical energy for fibre synthesis. In 1902, John William Strutt, also known as Lord Rayleigh, pioneered research on the behaviour of charged droplets during electrospraying, a concept that later became fundamental to the development of electrospinning. This phenomenon, known as Rayleigh instability, was further explored in depth by Zeleny in 1914, who expanded on Rayleigh's findings to deepen the understanding of this principle [36], [37], [38].

The publication of a series of patents by Formhals between 1934 and 1944, along with Taylor's groundbreaking research on electrically driven jets in 1969, significantly accelerated the development of the electrospinning process. Following these advancements, numerous research groups over the decades further studied and refined the technique. By the 1980s, electrospinning had gained widespread popularity due to its high reproducibility and ease of industrial-scale, cost-effective manufacturing [34], [37].

The principle of electrospinning begins with the application of an electric field to a liquid droplet of a solution as they are expelled from the tip of a fine orifice connected to a syringe, causing electrostatic charges to accumulate at its tip. At a distance, a grounded collector is placed to create a charge repulsion counteracts the surface tension, transforming the droplet from a spherical shape into an elongated cone, known as a Taylor Cone. From the tip of this cone, a jet of liquid is ejected through a capillary spinneret. While the jet often follows a complex, unstable path due to electric charge interactions, in the absence of a highly viscous polymer solution, the liquid eventually disperses into tiny droplets called beads. This process that underlies with the process of electrospraying. However, when the liquid contains a dissolved polymer, its viscosity plays a crucial role; if sufficiently high, the polymer viscosity prevents the jet from breaking into droplets, allowing fibre formation instead [34], [37].

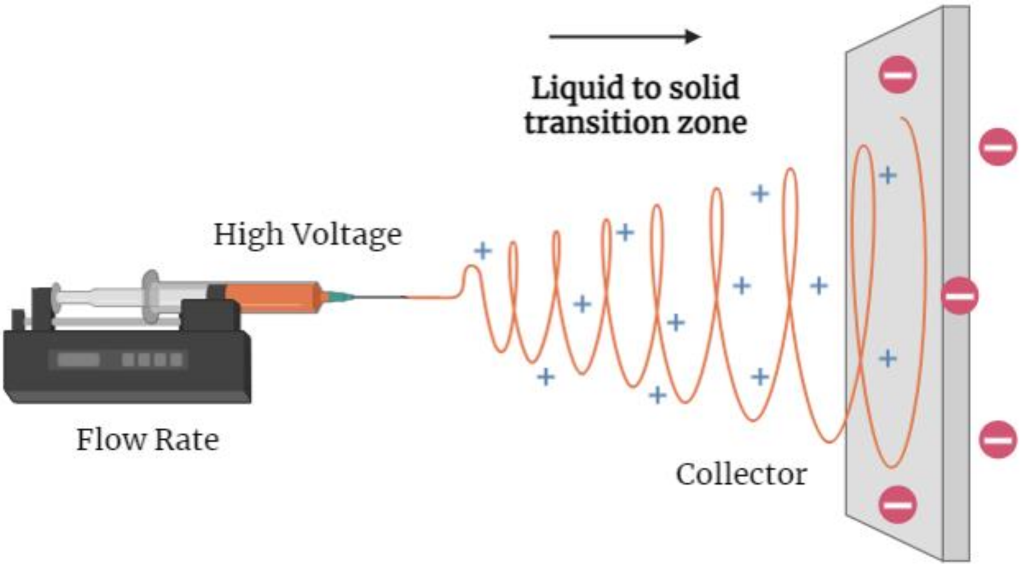

Figure 2.2.1: Electrospinning setup where positive high voltage is applied. Schematical illustration produced using Biorender® (Canada).

2.2.2 *Fabrication of Electrospun Meshes*

Electrospinning technology allows for the creation of ultrafine fibres that form a non-woven, scaffold-like structure, closely resembling the natural extracellular matrix found in many connective tissues. These meshes have proven effective in tissue engineering applications, facilitating the repair of bone, skin, blood vessels, cartilage, nerves and the damages done to abdominal wall such as a hernia [39], [40], [41], [42].

The creation of electrospun surgical meshes involves selecting a suitable polymer solution and subjecting it to the electrospinning process. To produce a fibre mesh, a significant volume of the polymer solution is needed to form a mat composed of layers of overlapping fibres. The production of electrospun meshes offers several advantages. One of the key benefits is the ability to select a polymer tailored to the specific requirements of the intended application [43]. Additionally, these meshes can be easily modified to meet various needs. The manufacturing process is often cost-effective, requiring minimal labour and allowing for scalability [34]. Moreover, electrospun meshes can be functionalized by incorporating drug delivery systems, gene and immunotherapy, antibacterial and anti-inflammatory agents, and cell growth factors, among other enhancements. This versatility makes them suitable for a wide range of applications in fields such as tissue engineering, wound healing, and regenerative medicine [39], [41].

2.2.3 *Synthetic and Natural Polymers for electrospinning fibres*

The selection of synthetic, natural, or a blend of both polymers, has a profound impact on the properties of the resulting fibres. Furthermore, it is important to note that the utilisation of a mixture of two polymers, referred to as a copolymer, can significantly influence the characteristics of the fibres produced. Choosing to employ a copolymer is an advantageous approach, as it allows for the integration of the unique properties of two distinct polymers into a single material. This not only enhances the mechanical and physical properties of the fibre mesh but also broadens its potential applications in the biomedical field [37], [43].

Synthetic polymers provide several advantages over their natural counterparts. Common synthetic polymers in electrospinning include polycaprolactone (PCL), polyglycolide (PGA) and polylactide (PLA) (*Table 2.2.1*). These polymers can be engineered to offer a wider array of characteristics, including tailored strength and viscoelasticity as well as controlled degradation rates. Nevertheless, some synthetic polymers can suffer from being susceptible to bacterial growth, reduced biocompatibility and prolonged biodegradation, which may limit their application in certain contexts [[42], [43], [44].

In contrast, natural polymers typically exhibit low immunogenicity and superior biocompatibility. They usually possess the capability to bind cells, offering promising clinical results, which makes them particularly relevant in tissue regeneration. Frequently used natural polymers used in electrospinning include chitosan, gelatine and silk. (*Table 2.2.1*) However, the use of natural polymers in electrospinning can present challenges, such as quicker degradation compared to their synthetic counterparts, partial denaturation and fabrication issues depending associated to the selected polymer. [37], [43]

Table 2.2.1: Some of the most commonly used polymers for electrospinning [37]

Polymer	Origin	Applications
Polycaprolactone (PCL)	Synthetic	Bone regeneration and tissue engineering
Polyglycolide (PGA)		Surgical sutures and bone regeneration
Polylactide (PLA)		Surgical sutures and plastic materials
Chitosan	Natural	Bone regeneration and tissue engineering
Gelatine		Gene delivery and bone regeneration
Silk		Wound repair and skin regeneration

In the case of copolymers when electrospinning, the performance of copolymer-based electrospun meshes can be significantly superior to those made from homopolymers. However, producing copolymer meshes for applications like hernia repair can be challenging due to their potentially higher hydrophobicity, which results from the large number of polyester bonds in the material. These polyesters bring strong mechanical properties to the product but, they typically lack cell affinity, which is important for tissue engineering applications. This issue can be addressed by incorporating a hydrophilic polymer component or segment, which improves cell compatibility. Additionally, copolymers allow for the customisation of fibre morphology, structure, biodegradability, and mechanical properties, further expanding their potential in electrospinning applications [37], [43].

Choosing the right polymer is not the only critical factor in preparing the polymer solution; selecting the appropriate solvent is equally important. Solvents must be chosen wisely. They must possess optimal boiling points, volatility, vapour pressure, solubility of the polymer and other key properties to ensure the integrity of the polymer solution. The solvent greatly influences both the morphology of the fibres and its spinnability [37].

2.2.4 *Polyhydroxybutyrate (PHB) as natural polymer for electrospinning*

Polyhydroxybutyrate belongs to the group of the polyhydroxyalkanoates (PHAs). PHAs are biopolyesters derived from 3-hydroxyalkanoic acids, synthesised and accumulated by bacterial cells as intracellular carbon and energy reserves in response to stress conditions. PHB is one of the most commonly observed forms of PHAs and is composed of tightly packed R-3-hydroxybutyrate (R-3-HB) monomers [45], [46], [47].

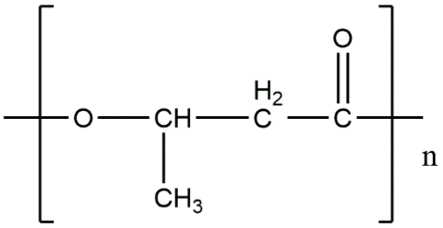

$$\left[-O-\underset{CH_3}{\underset{|}{CH}}-\overset{H_2}{C}-\overset{O}{\overset{\|}{C}}- \right]_n$$

Figure 2.2.2: Poly[®-3-hydroxybutyric acid] chemical structure. Chemical Structure drawn using ChemDraw® online software.

PHB is a carbon-based biodegradable, highly biocompatible, hydrophobic, non-toxic, biopolymer. The benefit of using of a biodegradable polymer in electrospinning is that it creates fibre matrices, which offers numerous advantages, with the most significant being their ability to biodegrade into oligomers and monomers that can be metabolized through normal physiological pathways. However, one notable disadvantage is their considerably higher cost compared to conventional petroleum-based polymers. Despite this, PHAs exhibit great potential in drug delivery and tissue engineering due to their excellent biocompatibility and *in vivo* degradability. The most extensively studied PHAs include poly(3-hydroxybutyrate) (PHB) and its co-polymer poly(3-hydroxybutyrate-co-valerate) (PHBV), which are commercially available [47], [48].

2.3 Nanotechnology in Medical Devices

2.3.1 *Role of Nanotechnology in Enhancing Materials*

To explain the role of nanotechnology in enhancing materials used in medical devices, first, we must define medical devices. Medical devices (MDs), according to the definition provided by the World Health Organization (WHO) [49], are any instrument, software, appliance, implant, reagent for *in vitro* use, material, or related article intended by the manufacturer for human consumption for one or more specific medical purposes [50], such as:

- Diagnosis, prevention, monitoring, treatment, or alleviation of disease or an injury.
- Investigation, replacement or modification of anatomical structures or physiological processes.
- Supporting or sustaining life and contraception.
- Disinfection of medical devices.
- Providing information through *in vitro* examination of specimens derived from the human body.

They serve as an essential tool for the diagnosis, prevention, monitoring, and treatment of distinct medical conditions, while also enhancing patie’ts' quality of life [50].

The concept of nanotechnology was first introduced in 1959 by physicist Richard Feynman, who proposed the innovative idea of producing materials and manipulating matter at the atomic and molecular levels. It can be defined as a scientific discipline focused on phenomena that occur at the nanoscale. It encompasses the synthesis, characterization, and production of various devices, systems, and structures for a wide range of applications across multiple fields in the ^{2}1st century, nanotechnology is recognized as a promising field, opening new avenues for research in medicine and materials science [51]

The concept of nanotechnology was first introduced in 1959 by physicist Richard Feynman, who proposed the innovative idea of producing materials and manipulating matter at the atomic and molecular levels. In the 21st century, nanotechnology is recognized as one of the most promising fields, opening new avenues for research in medicine and materials science [51].

Nanotechnology plays a vital role in several medical fields, including wound care, antibacterial treatments, preventative medicine, and diagnostic procedures, where different types of nanomaterials are utilised. The table below provides an overview of the most common types of nanomaterials used in medical applications, highlighting their applications and characteristics [51], [52].

Table 2.3.1: Most common types of nanomaterials and their characteristics in the medical field [52].

Types	Examples	Size	Applications	Reference
Nanodots (NDs)	Carbon-based.	1 to 10 nm.	Detection of metal ion17iomoleculesles, drug molecules, drug delivery, antibacterial applications and bioimaging.	[52], [53]
Nanoparticles (NPs)	Polymeric. Carbon-based. Metal-based. Lipid-based.	1 to 100 nanometres.	Drug delivery, gene delivery, biosensing and bioimaging.	[54]
Nanogenerators	Triboelectric Piezoelectric Pyroelectric	Varies, nanometres to centimetres.	Could self-power nanodevices and nanosystems to provide movement, such as muscle movement.	[55]
Nanotubes (NTs)	Carbon-based. Silicon. Gallium.	Up to 20 nm.	Pesticides, drug delivery and nanofiltration.	[56]
Quantum Dots (QDs)	Carbon-based. Bismuth-based.	2-15 nm.	Bioimaging, diagnostics, and drug delivery.	[52]

Regarding hernia repair, in recent years, research has increasingly concentrated on the development of bioengineered meshes and wound repair scaffolds that mimic the diverse characteristics of the native extracellular matrix (ECM). Notably, these nanotechnology-based medical devices offer superior surface-to-volume ratios, enabling them to engage deeply with the biological targets at the damaged tissue on sight [51].

2.3.2 *Antimicrobial Strategies Using Nanomaterials in Surgical Meshes*

In recent years, infectious diseases caused by bacteria and bacterial biofilms, such as pneumonia, meningitis, sepsis, and chronic infections, have emerged as a significant threat to global public health. Since the discovery of penicillin in 1923, antibiotics have played a crucial role in clinical practice, effectively saving patients by preventing infections that were once lethal. However, the misuse and overprescription of antibiotics have led to the emergence of antibiotic-resistant strains, which are now commonly found in hospitals [57].

The prevalence of infections caused by drug-resistant bacteria is rising alarmingly, unfortunately, coinciding with the present antibiotic resistance crisis. Prolonged or excessive use of broad-spectrum antibiotics can disrupt or eliminate beneficial normal bacterial strain populations in a human being, resulting in a weakened immune system. Many pathogenic bacteria not only exhibit inherent resistance to antibiotic treatment but also increasingly acquire resistance to multiple antibiotics, significantly diminishing treatment efficacy or rendering it ineffective altogether [57]. In a hospital environment, patients acquire these infections after a major surgical procedure, usually presented in the form of surgical site infection or urinary site infection, increasing the hospitalisation duration of their stay from 2 to 7 days up until 30 days [58], adding to additional costs that the patient did not have considered.

Therefore, to treat this emergent increase on infections, specifically in surgical site infections and nosocomial infection, measures have been taken to prevent infection in all fields, including hernia repair. These measures include the use of meshes that have been functionalised into including nanomaterials that provide an antibacterial effect [59], [60], [61]

In contrast to traditional antibiotics, nanomaterials offer a range of intrinsic passive antibacterial mechanisms that specifically target biological sites affecting within or on the outer shell of the bacterial cells, thereby reducing the likelihood of resistance. Nanotechnology has been studying this occurrence and continues to advance and integrate into the field of antimicrobials, as viable biological alternatives to antibiotics [57], [62], [63].

Novel antibacterial agents based on nanomaterials has progressed rapidly over the past decade. These agents provide several advantages, such as broad-spectrum antimicrobial activity, high efficacy, and low toxicity to the patient, but most relevantly they also employ multiple mechanisms to synergistically enhance their antimicrobial effects, effectively reducing over time the rise of bacterial resistance. To give an example, nanomaterials can exert their antimicrobial properties through direct physical interactions with bacterial cells, such as the release of reactive oxygen species (ROS), either directly or indirectly [64].

Furthermore, the ability to be able to empirically adjust and optimise the physicochemical properties of these nanomaterials makes them highly desirable for use in in clinical research to be, later on, able to release them to the public. This versatility enables them to meet the specific requirements of different antibacterial applications and strains effectively [64], [65].

In the case of medical meshes, one of the most critical areas of research focuses on biofilm-forming bacteria. According to estimates from the NIH and CDC, these bacteria are responsible for over 60% of nosocomial infections. Nosocomial infections pose significant risks in healthcare, contributing to chronic infections related to implanted medical devices, surgical-placed mesh implants, intravenous access line-induced bloodstream infection, and orthopedic procedures [64], [65].

Given the severity of these infections, various strategies have been investigated to mitigate the threats posed by these persistent pathogens. One promising approach involves using nanomaterials to disrupt the metabolism and signalling of cyclic dimeric guanosine monophosphate (c-di-GMP); this molecule that acts as a second messenger in bacterial processes, including biofilm formation [64], [65].

2.3.3 *Light Activated Carbon nanodots (CNDs) for Antimicrobial Applications*

Carbon nanodots (CNDs) are classified as nanoparticles with an amorphous, crystalline or semicrystalline core structure, which are easy and cost-effective to synthesise. They are smaller than traditional nanoparticles, ranging from 1-10 nm. At this size, they exhibit quantum confinement and fluorescence properties, similarly to quantum dots; nevertheless, carbon nanodots are primarily composed of carbon. They may have additional surface functional groups, but their core is typically made of carbon-based materials when they go through a process called doping, while quantum dots are typically made from semiconductor materials

Some advantaged that carbon nanodots offer are bright luminescence, low cytotoxicity, high biocompatibility, and tunable emission properties, making them highly versatile for various applications (*Figure 2.3.1*) [53].

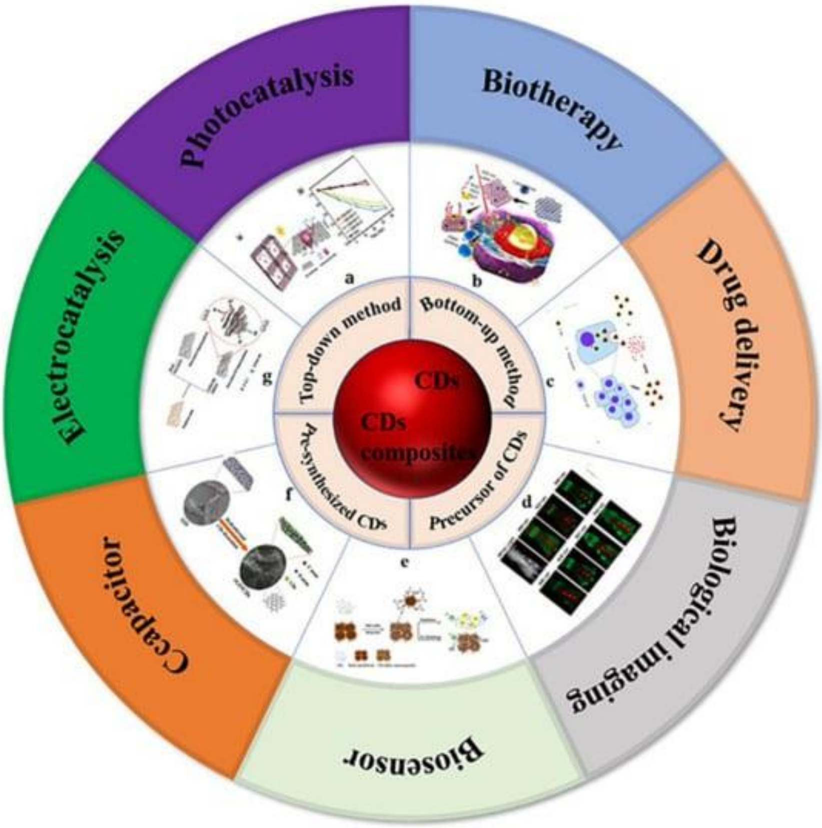

Figure 2.3.1: Different applications for C-dots and their possible synthesis method. (Chai *et al*, 2022) Sourced from: [66].

CNDs are a novel class of carbon-based nanomaterials. They are gaining attention due to their unique electronic properties and the simplicity of their synthesis methods. This ease of synthesis sets CNDs apart from other materials, which often require more complex and labor-intensive processes. During synthesis, the sp^2 hybridized carbon core structures, along with functional groups like carboxyl, hydroxyl, amine, between others, depending and being obtained from both the precursor and activating agents [53], [66]

Furthermore, researchers have made significant progress in enhancing the tunability of the fluorescent properties of CNDs, positioning them as excellent alternatives to high-performance, more toxic nanomaterials, such as inorganic nanoparticles and quantum dots. CNDs offer strong chemical inertness, tunable photoluminescence, and minimal environmental impact. Additionally, their antibacterial properties are activated by prolonged exposure to light, typically in the ultraviolet range. However, there are exceptions where carbon nanodots are activated by light in the visible spectrum, allowing them to be employed for direct biomedical and clinical applications [53], [66] The origins of the characteristic fluorescence and the molecular insights of the CNDs has been studied vastly by researchers in order to understand the antibacterial capability and this has caused current debate amongst the research community. To date, factors such as multichromophoric regions, doping elements (when occurred), core structures, passivating molecules, and a wide variety of sizes are widely accepted as models for the fluorescence origins in most optical studies of CNDs [53].

Additionally, properties such as solvation and fluorescence polarisation are vital for CNDs. CNDs also exhibit anisotropic behaviour, similar to quantum rods, meaning their properties can differ based on direction, indicating a more robust and durable structure. Furthermore, recent studies have shown that low temperatures can significantly influence various organic segments, therefore, affecting the fluorescence [53], [67].

Furthermore, on the optical properties of the CNDs and photoluminescence, certain carbon nanodots have the capacity to perform antibacterial inactivation on light command. This ability occurs due to a process called antimicrobial photodynamic inactivation (aPDI). This technique utilises a non-toxic photosensitiser combined with light illumination to generate antimicrobial reactive oxygen species (ROS) from environmental oxygen. The ROS can form through two primary mechanisms: one mechanism produces hydroxyl radicals, superoxide, or hydrogen peroxide, while the other generates singlet oxygen ($^1O_2$) [8], [53], [68]

These species react non-specifically with cellular or viral components, resulting in significant oxidative damage that effectively inactivates a wide range of microbial agents, including bacteria, viruses, fungi, and even parasites [60], [61]. This inactivation through ROS-mediated oxidative damage has notable advantages [53], [69]:

- Microorganisms that resistant to traditional antibiotics are inactivated at levels comparable to their drug-susceptible counterparts.
- Since it is non-specific damage caused by ROS makes the development of resistance highly unlikely.

These benefits make proxylaxis techniques using aPDI particularly appealing for preventing the spread of nosocomial and surgical site infections from drug-resistant pathogens [53]. However, these materials can also provide other applications, such as the disinfection of surfaces and materials for sterilisation purposes.

Despite these remarkable advantages, in the case of a clinical hernia application it must be noted that the activation should be realised with carbon nanodots that provide cell proliferation properties or at least good cytocompatibility and they must be activated in prophylaxis opportunities as well as for surgical site infection (SSI) treatment [8], [64].

Nonetheless, while antimicrobial photodynamic inactivation (aPDI) offers several advantages, it is important to emphasize that it is a non-specific technique. This means it can affect healthy tissue surrounding the infection while also reducing the bacterial population [8], [69]. Despite this limitation, carbon nanodots have demonstrated significant potential in anti-cancer photodynamic therapies due to their excellent cytocompatibility, high biodegradability, and water solubility, which reiterates that harm is minimal if performed correctly.

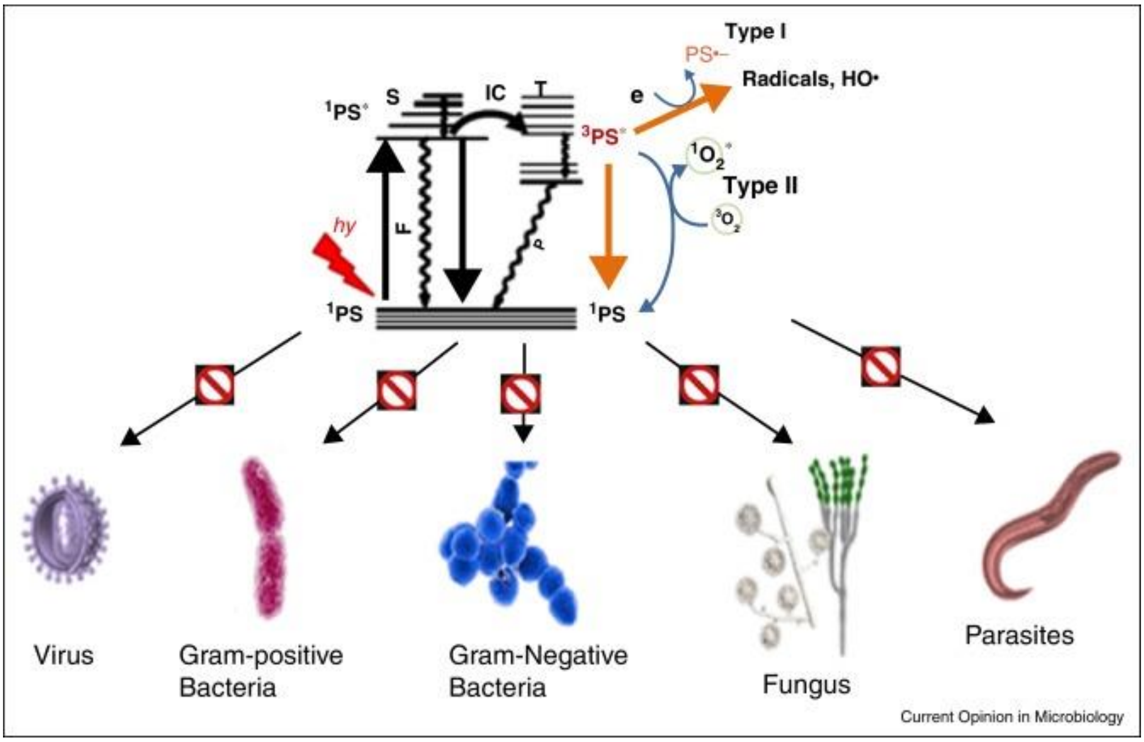

Figure 2.3.2: Jablonski Diagram of aPDI Mechanisms (Haleen, 2023) Sourced from: [51].

Chapter 3

Materials and Methods

3.1 Materials

The materials and reagents shown in Table 3.1.1 were used for electrospinning of Coaxial PHB and PHB/CND fibres.

Table 3.1.1: Coaxial electrospinning of PHB solution as the Core Solution and PHB/CND solution as the Shell Solution, materials and reagents.

Generation of solution	Product	Supplier	Catalogue number
PHB and PHB/CND solution	Chloroform	Sigma-Aldrich, USA	C2432
	Poly[(R)-3-hydroxybutyric acid]		363502
PHB/CND solution and CND solutions	Citric acid		251275
	1,5-Diaminonaphthalene		D21200
CND solution before freeze-drying	Ethanol		34852-M
	Whatman® UNIFLO® 25 syringe filters		WHA9914-2502

3.2 Methods

3.2.1 *Carbon nanodots (CNDs) Synthesis*

CNDs were synthesised according to [70], using a one-pot solvothermal method with the mass ratio of citric acid to 1,5-diaminonaphthalene of 1:2. 1,5-DAN (260 mg, 1.64 mmol) and CA (130 mg, 0.68 mmol) were added to absolute ethanol (130 mL). This solution was subjected to ultrasonic bath treatment at 80 kHz Frequency (Fisherbrand™ 112xx Series Advanced Ultrasonic Cleaner, Fisher Scientific, USA) for 10 minutes until suspended and then transferred into an oven, where it was heated at 200°C for 9h. Afterwards, the solution was subjected to rotary evaporation to remove the ethanol. Subsequently, the particles were resuspended in water. The resulted product was filtered using a Acrodisc 0.2 µm Membrane Syringe Filter (Sigma-Aldrich, USA) and went through tip sonication for 5 minutes with the conditions of 10% amplitude and one second pulse-on and pulse-off timing. Finally, the solution was freeze-dried for 3 days to obtain dark purple-brown CND particles.

3.2.2 *Electrospinning solutions preparation (PHB and PHB/CND Solutions)*

3.2.2.1 *PHB and PHB/CND Solutions for coaxial electrospinning*

The PHB Solution without the addition of CNDs was carried out by dissolving poly[(R)-3-hydroxybutyric acid] (PHB) in chloroform to make a 10%wt solution (1 g/10 mL). The solution was stored in a glass vial with a sealed lid to prevent evaporation and was stirred continuously using a magnetic stirrer in an oil bath at 55°C for 1 hour.

The PHB/CND solutions were produced by weighing different concentrations of CNDs. 10 mg, 25 mg, 50 mg and 100 mg (1%, 2.5%, 5% and 10%w/v) of the previously synthesised CNDs were added into a glass vial with a sealed lid (*Table 3.2.1*). Afterwards, 2 mL of chloroform were added to create a suspension. This suspension is subjected to 5 minutes of ultrasonic bath treatment at 80 kHz Frequency (Fisher Scientific, USA) and following this, 500 mg of PHB powder and 8 mL of chloroform are added to them to make a 5%wt PHB solution in 10 mL. The solution was stirred continuously using a magnetic stirrer in an oil bath at 55°C for 1 hour.

Table 3.2.1 Weights and volumes used to prepare PHB and PHB/CND solutions.

CNDs Percentage in sample (w/v)	CNDs weight (g)	PHB percentage in sample (wt)	Chloroform volume (mL)
0	0	10	10
1	10	5	
2.5	25		
5	50		
10	10		

3.2.2.2 *PHB Solution for single needle electrospinning, for comparison*

The solution was synthesised in the same manner as the PHB solution for coaxial electrospinning where, poly[(R)-3-hydroxybutyric acid] (PHB) was dissolved in chloroform to make a 10%wt solution (1 g/10 mL). The solution was stored in a glass vial with a sealed lid to prevent evaporation and was stirred continuously using a magnetic stirrer in an oil bath at 55°C for 1 hour.

3.2.3 *Electrospinning Setup and Parameters for coaxial electrospinning*

A horizontal setup was used to carry out the electrospinning experiments. The PHB and PHB/CND solutions were loaded onto a 10 mL disposable plastic syringes connected to a blunt-ended metal coaxial needle (18G inner diameter, 14G outer diameter, Vita Needle, USA). Each syringe was then attached to two programmable syringe pump drivers, where each independently controls the flow of the solutions out of the syringes to become the core (18G) and shell (14G) portion of the fibres. The rate of solution flow was controlled by the syringe pump driver (NE-300, New Era, USA) at 0.25 mL/h and the tip of the needle was connected to a clamp that carries the high voltage. A ground wire clamp was connected to a bespoke 3D printed rotating drum used as a collector (10 cm in diameter), configured at a speed of 400 rpm, covered by aluminium foil to collect the fibres (*Figure 3.2.1*). For safety, the electrospinning setup is placed in a designated cupboard grounded throughout. The distance between the needle tip and the collector was set at 12 cm. After doing voltage screening between –10 kV to –25 kV, it was determined that –21 kV was optimal. After the electrospinning process concludes, the aluminium foil was collected and afterwards cut into 5x10 cm pieces and stored to avoid light exposure.

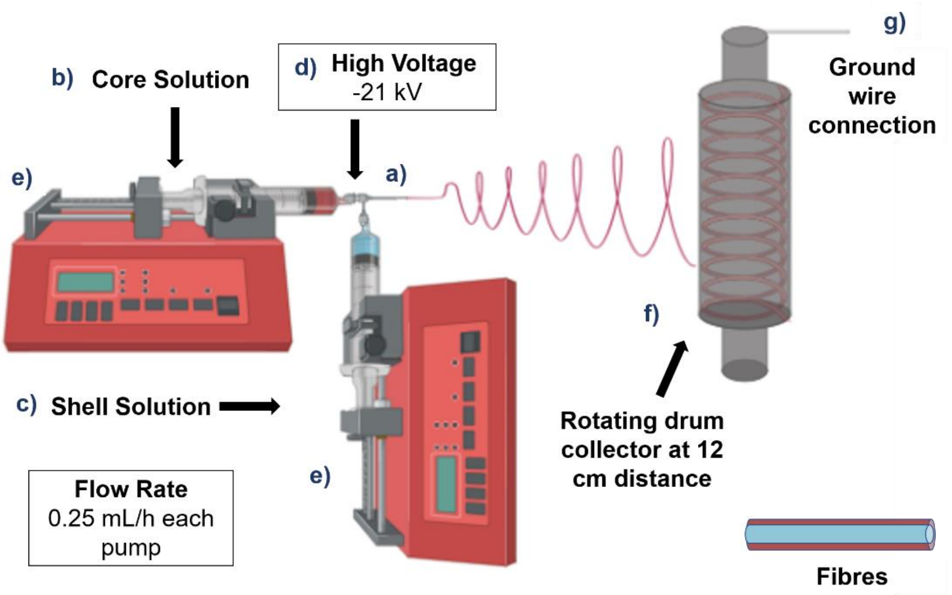

Figure 3.2.1: Electrospinning set-up used. a) coaxial needle b) syringe containing PHB solution (core solution), c) syringe containing PHB/CND solution (shell solution), d) high voltage wire connection, e) syringe pump driver controlling outflow of solution from needle towards, f) a rotating collector covered in aluminium foil with g), ground wire connection. Schematical illustration produced using Biorender® (Canada).

3.2.4 *Electrospinning Setup and Parameters for single needle electrospinning*

The single needle electrospinning setup was similar to that of the coaxial needle electrospinning system, except that in this setup, the PHB solution were loaded onto a single 10 mL disposable Luer Lock plastic syringe (Fisher Scientific, USA) connected to a blunt-ended metal disposable needle (21G inner diameter) (AGANI Needle, Japan). The syringe was then attached to a single programmable syringe pump driver (NE-300, New Era, USA). The pump rate was set at 0.5 mL/h. After doing the voltage screening between –10 kV to –25 kV, it was determined that –18.5 kV was chosen for the single needle electrospinning. Additionally, the distance between the needle tip and collector (12 cm), the position of the voltage and grounding clamps remained the same as the coaxial electrospinning setup (*Figure 3.2.2*). The designated cupboard was used and after the electrospinning process concludes, the aluminium foil was collected and cut into 5x10 cm pieces and stored avoiding light.

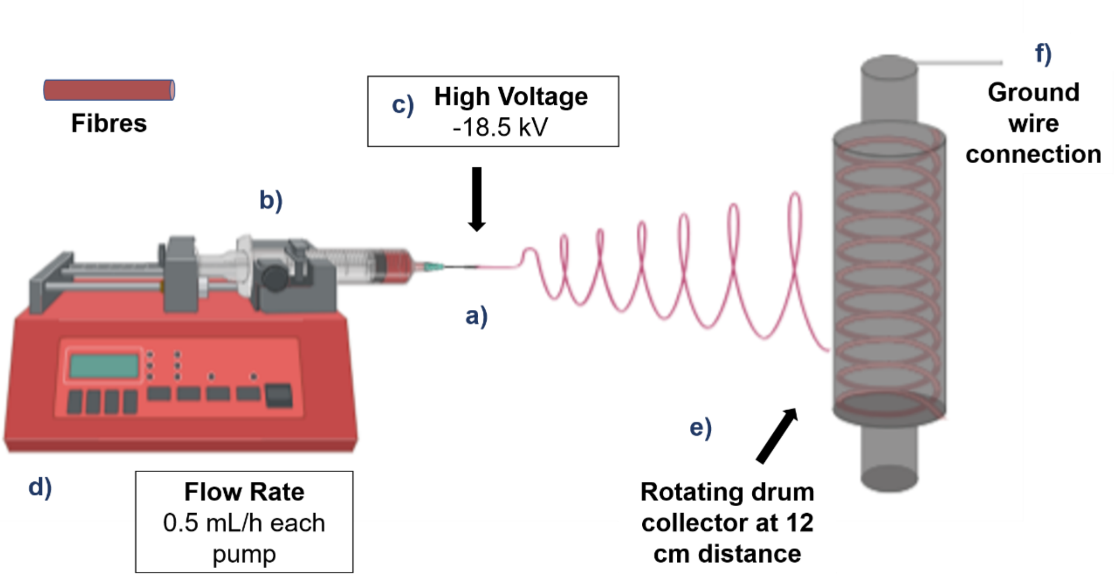

Figure 3.2.2 Electrospinning set-up used. a) needle b) syringe containing PHB solution, c) high voltage wire connection, d) syringe pump driver controlling outflow of solution from needle towards, e) a rotating collector covered in aluminium foil with f), ground wire connection. Schematical illustration produced using Biorender® (Canada).

3.3 Characterisation

3.3.1 *Scanning Electron Microscopy (SEM)*

Scanning Electron Microscopy (SEM) was employed to evaluate the architecture of the mesh and the formation of core-shell fibres. A scanning electron microscope (FEI Inspect F, FEI Company, Oregon, USA) located in the Nanovision Centre, Queen Mary University of London, was utilised for this purpose. Samples were prepared by cutting them into circular shapes with a radius of 1 cm and mounting them onto adhesive carbon-coated metal stubs. Subsequently, the specimens were sputter-coated with a 10 nm layer of gold-palladium using an Agar auto sputter coater (Agar Scientific Ltd, UK). Micrographs were captured at a high voltage of 10 kV, a working distance of 10 mm, a spot size of 3.5 and an aperture setting of 6 for imaging. For Energy Dispersive X-ray spectroscopy (EDS) analysis, micrographs were taken at the same voltage and working distance, but with a spot size of 4.5 and an aperture of 4. Additionally, SEM micrographs were analysed to determine the average fibre diameter and distribution using ImageJ® software (NIH, USA).

3.3.2 *Transmission Electron Microscopy (TEM)*

TEM microscopy was used to identify the core-shell structure coaxial fibres and the morphology and arrangement of the carbon nanodots. Sample was prepared using the drop casting method, where the sample was placed on Lacey carbon films on Copper TEM Grids (Agar Scientific, UK). The samples selected were prepared using two methods:

- For the CNDs, a 10 mg/mL solution was prepared with ultrapure deionised water and subjected to an ultrasonic bath at 80 kHz Frequency (Fisher Scientific, USA) for 5 minutes. The solution was then filtered using an Acrodisc 0.2 µm Membrane Syringe Filter (Sigma-Aldrich, USA). The drop casting method was performed using a micropipette with 20 µL of the solution and dropping it on the copper TEM grid, leaving it to dry overnight.
- For the coaxial fibres, a small 1 mg weight piece was cut and placed in a glass vial containing 5 mL of acetone. Afterwards, the solution containing the dispersed fibres was subjected to ultrasonic bath treatment at 80 kHz Frequency (Fisher Scientific, USA) for 5 minutes. The drop casting method was realised using a micropipette with 20 µL of the solution and dropping it on the copper TEM grid.

The samples were then imaged using a JEM-F200 Multi-purpose Electron Microscope (JEOL, Japan) at an accelerated voltage of 200 kV in emission with a Spot size of 1. TEM imaging was performed at the NanoVision Centre in Queen Mary, University of London.

3.3.3 *Dynamic Light Scattering (DLS)*

Particle size measurement was analysed using a Malvern Nano ZS SERIES Zetasizer. (Malvern Panalytical, UK). The carbon nanodots dispersed in ultrapure deionised water were analysed using a disposable Polystyrene Cuvettes for UV and Visible Wavelengths (Fisherbrand™ FB55923, Fisher Scientific, USA) with a wavelength analysis range from 340-900 nm. The concentration determined to analyse the sample was 0.5 mg/mL, dispersed for 3 minutes in an ultrasonic bath treatment at 80 kHz Frequency (Fisher Scientific, USA).

3.3.4 *ATR-FTIR Spectroscopy*

This measurement was chosen to be able to confirm the formation of the composite fibres and compare the spectras for different additions of CNDs. The FTIR spectra were documented using a Bruker Tensor 27 FTIR spectrometer (Bruker, USA) with an ATR accessory. The samples were tested directly on the equipment. Transmittance mode was utilised to measure the samples and scans were acquired across the 4000–400 cm^{-1} wavenumber range at a resolution of 4 cm^{-1} with 16 scans performed per spectrum. These scans were later analysed using the equipment's OPUS® software (Bruker, USA). 7 samples were tested: the CNDs, PHB powder for comparison, 0%, 1%, 2.5%, 5% and 10% of added CNDs fibre meshes.

3.3.5 *UV-Vis Spectroscopy*

UV-Vis Spectroscopy analysis was taken with a Perkin Elmer Lambda35 UV-vis spectrometer (Perkin Elmer, USA). This equipment has a scanning double-beam spectrometer. The sample selected was the carbon nanodots alone and they were dispersed in ultrapure deionised water were analysed in a wavelength range from 190 - 1100 nm using a UV quartz cuvette (Sigma-Aldrich, USA). The concentration determined for use was $5x10^{-5}$ mg/mL.

3.3.6 *Fluorescence Spectroscopy*

The fluorescence analysis was taken using a Perkin Elmer LS55 spectrofluorometer with Xenon pulsed flash lamp (Perkin Elmer, USA). The carbon nanodots were dispersed in ultrapure deionised water were analysed in a wavelength range from 200-650 nm using a Hellma® Fluorescence quartz cuvette (Sigma-Aldrich, USA). The chosen excitation wavelength for the sample was λ_{ex}= 300 nm. The concentration used was $1x10^{-12}$ mg/mL.

3.3.7 *Contact Angle Measurement of Sessile Drops/Drop Shape Analysis*

Contact angle measurements were taken of the 0%, 1%, 2.5%, 5% and 10% added CNDs synthesised fibres as well as the CNDs sample. This was carried out at room temperature. A 10 µl sized droplet of ultrapure deionised water was dropped on the mesh and CNDs surface. Contact angles were determined using an Kruss DSA100 drop shape analyser (KRUSS Scientific, Germany).

3.3.8 *Thermogravimetric analysis (TGA)*

Thermogravimetric analysis (TGA) was conducted on 0%, 1%, 2.5%, 5% and 10% of added CNDs synthesised fibres as well as CNDs to determine the degradation temperature of each product. Samples weighing 2-6 mg were placed in the TGA equipment (TGA 5500, TA Instruments, USA), and thermal degradation was carried out under nitrogen gas supply from room temperature to 900ºC for the fibre meshes and from room temperature to 1000°C for the CNDs at a heating rate of 10°C/min. All data are presented as temperature versus weight change.

3.3.9 *Differential scanning calorimetry (DSC)*

Differential scanning calorimetry (DSC) was performed on 0%, 1%, 2.5%, 5% and 10% added CNDs synthesised fibres as well as the CNDs to determine the temperature-related transitions of each product before the degradation temperature. Samples weighing between 2-6 mg were placed in the DSC equipment (DSC 25, TA Instruments, USA), and the procedure was carried out under nitrogen gas supply from -5°C to 230ºC for all the samples at a heating rate of 5°C/min. It was decided to use a cyclic procedure, where two cycles were performed for comparison. All data were presented as temperature versus Normalized Heat Flow (W/g).

3.3.10 *X-ray photoelectron spectroscopy (XPS) Analysis*

X-ray Photoelectron Spectroscopy (XPS) was employed to characterise the chemical elements present on the surface of the single needle and coaxial synthesised fibres (0%, 2.5% and 10% addition of CNDs on mesh) and the synthetised CNDs. X-Ray Photoelectron Spectroscopy (XPS) was carried out on a Thermo Scientific, Nexsa® spectrometer under UHV at ambient temperature. XPS results were analysed using Avantage® software. (ThermoFisher, USA), with a micro-focused X-ray source at 100 µm.

3.3.11 *MTT Assay using L-929 cell line*

The cell line utilised for the experiment was L-929 cells obtained from Sigma-Aldrich (USA, catalogue number CCL-1). These cells are a murine fibroblast cell line which is commonly used for cytotoxicity studies. The experiments were performed in a sterilised Class II Biological safety cabinet (Mars, Labogene, Denmark) and left for incubation periods on a Binder CO_2 Incubator model C150 from Binder GmbH (Germany).

The reagents used in the analysis of 0%, 1%, 2.5%, 5% and 10% of added CNDs in the fibre meshes experiments are listed in *Table 3.3.1*.

Table 3.3.1: Reagents utilised during the cell culture experiments.

Product	Supplier	Catalogue number
Cell culture flasks T-75 (75 cm^2)	Thermo Fisher Scientific, USA	156499
Dulbecco's Modified Eagle's Medium, low glucose (DMEM)	Sigma Aldrich, USA	D6046
Ethanol	Honeywell, USA	24194
Foetal Bovine Serum (FBS)	Sigma Aldrich, USA	F9665
Penicillin-Streptomycin (P/S)		P4333
Phosphate Buffered Saline	Thermo Fisher Scientific, USA	D8537
Sterilin X700 container aseptice 7 mL no label	Fisher Scientific, USA	12799985
Trypan blue solution, 0.4%	Thermo Fisher Scientific, USA	15250061
TrypLE™ Express Enzyme		12604021
12-well Clear TC-treated Multiple Well Plates	Fisher Scientific, USA	10253041
96-Well, Cell Culture-Treated, Flat-Bottom Microplate		10695951

The L-929 cell line (mouse fibroblast cell line) was used as it is established in continuous culture and a well-known cell line for cytotoxicity testing of biomaterials. The L-929 cells was employed to assess the cytotoxicity of the fibre meshes, as the use of this cell line is recommended in ISO 10993, Part 5, Annex C: MTT cytotoxicity test [50]. Cells were cultured from passage 5-7 and kept in sterile conditions in a CO2 incubator. The L-929 cells were cultured in a media solution containing 79% Low-Glucose Dulbecco's Modified Eagle's Medium (DMEM) supplemented by 20% foetal bovine serum (FBS) and 1% Penicillin/Streptomycin (P/S) in T-75 flasks. Cells were incubated at 37°C at 5% CO2 until approximately 80-90% confluency was reached. Media was changed every 2-4 days.

Once confluency was reached, the cells were harvested utilizing TrypLETM Express Enzyme and manually counted using a haemocytometer using 10 µL Trypan blue and 10 µL of the suspension of cells. After this procedure, L-929 cells were seeded into 96-well plates with a 50µl cell suspension in each well, at a concentration of 1x105 cells/mL. Subsequently, the cells were incubated at 37°C at 5% CO2 for 48 hours.

3.3.11.1 *Sample preparation and sterilisation*

Electrospun fibre mesh material with the addition of 0%, 1%, 2.5%, 5% and 10% of CNDs were manually cut into 1cm^2 samples and with an approximate weight of 5 mg. They were sterilised using a solution of 70% v/v ethanol (Honeywell, USA). Samples left on the solution inside the Class II Safety Cabinet (Mars, Labogene, Denmark) in a sterile environment and left to dry overnight. Dried samples were then subjected to an hour of UV light irradiation to sterilise them.

3.3.11.2 *Mesh wetting*

To realise the wetting process, triplicates of the different concentrations of the fibre mesh were used (0%, 1%, 2.5%, 5% and 10% added CNDs). The triplicates were placed in a 7 mL sterile container (Fisher Scientific, USA), to which 5 mL of the media solution were added. Full wetting of the product at room temperature was necessary for the MTT Assay. The meshes tended to float due to its hydrophobic nature but would remain submerged after they were completely wet and they did not degrade during the maximum of 72 hours of culture. This was intended to be able to compare if, in an application, it would be beneficial to place the mesh in the patient immediately or if it would be necessary to pretreat it to ensure that all the solvents were eliminated. Therefore, 4 sample testing groups were designated (*Table 3.3.2*).

Table 3.3.2: Different time durations for submerging the fibre samples.

24D (24 hours, no media change)	**72D** (72 hours, no media change)	**24C** (24 hours, media change)	**72D** (72 hours, media change)
Mesh was placed in the container and incubated at 37°C at 5% CO_2 for 24 hours. Afterwards, the mesh was removed and the media was stored in the fridge until further analysis.	Mesh was placed in the container and incubated at 37°C at 5% CO_2 for 72 hours. Afterwards, the mesh was removed and the media was stored in the fridge until further analysis.	Mesh was placed in the container and incubated at 37°C at 5% CO_2 for 24 hours. Afterwards, the media inside the container was aspirated and the same volume of new media was added. After 24 hours of incubation, the mesh was removed and the media was stored in the fridge until further analysis.	Mesh was placed in the container and incubated at 37°C at 5% CO_2 for 72 hours. Afterwards, the media inside the container was aspirated and the same volume of new media was added. After 72 hours of incubation , the mesh was removed and the media was stored in the fridge until further analysis.

3.3.11.3 *MTT Assay Procedure after sample conditioning*

The previously produced test media eluted from the meshes was warmed up to 37ºC and placed in a sterile environment in a Class II Safety Cabinet (Mars, Labogene, Denmark). The 96-well plates with cells were examined in the microscope and when 80-90% confluency was reached, the remaining media was aspirated carefully and then 100 µL of the test media (*Table 3.3.2*) was added into each well. A triplicate of positive control cells was made, where DMEM media was added. Following this, all the plates were left to incubate at 37ºC for 24 hours.

After this period, the test media was discarded along with the DMEM media and SDS via aspiration. After this, 50 µL of serum-free media and 50 µL of MTT Reagent were added into each well where the test media, the positive control was placed using a multichannel pipette (VWR, USA). For background control wells, 50 µL MTT Reagent and 50 µL cell culture media was added (no cells). The plates were incubated at 37°C and 5% CO_2 for 3 hours. After incubation, 150 µL of MTT Solvent was incorporated into each well, as directed by the assay protocol [71], [72]. The plates were wrapped in aluminium foil and placed on an orbital shaker for 15 minutes (GyroTwister™ 3D Laboratory Orbital Shaker, Labnet, USA). Thereafter, the plates were read in absorbance mode at OD=590 nm at room temperature using the SPECTROstar Nano plate reader (BMG LABTECH, Germany). The data was later analysed using Mars software (BMG LABTECH, Germany).

When calculating cell viability in an MTT assay with adjustments for background (no cells), the formula needs to account for this factor to provide a more accurate representation of live cell viability. It was calculated in this manner:

$$Corrected\ data = Raw\ data\ (Sample\ or\ Positive\ Control) - Background$$

Where:

- The sample is the cells subjected to the experimental test media.
- Positive control refers to the live cells that were not subjected to the test media.
- Background means a well with no cells, just media.

Moreover, the formula for calculating percentage viability adjusted with the background [71], [73], is represented as:

$$Cell\ Viability\ (\%) = \left(\frac{Sample\ \ (Corrected)}{Positive\ Control\ (Corrected)}\right)\ x100$$

A product is considered to be a potentially cytotoxic if cell culture viability decreases to less than 70% compared to the positive control, which was designated with 100% viability according to ISO 10993, Part 5, Annex C: MTT cytotoxicity test [39]. The average viability percentages for each group were then calculated based on the results from three repetitions of each experiment and results were using GraphPad® Prism Software (USA).

Chapter 4

Material Synthesis and Characterisation

4.1 Introduction

The technique of electrospinning can be considered to be one of the most widely used methods to produce fibres with a uniform structure at the determined optimised electrospinning parameters. Hence electrospinning is a widely used technique in the industry for the fabrication of fibres from diverse materials and applications [34], [74]. Nonetheless, there are many variables that may affect the electrospinning process which, in response, may affect the morphology of the spun fibres. The electrospinning process was optimised in the polymer concentration and core-shell arrangement for the coaxial fibres. The aim was to synthesise single needle electrospun PHB fibre meshes to compare to coaxial PHB fibre meshes, where the shell structure of the coaxial fibres would have different concentrations of added CNDs in them for comparison. 2.5% of added CNDs would be the ideal since according to literature [70], this concentration is enough to kill bacteria on light command. 1%, 5% and 10% were used for comparison.

4.2 Synthesis: Results and Discussions

4.2.1 *Carbon nanodots (CNDs) Synthesis*

The CNDs were a dark purple-brown colour after lyophilisation. When suspended in water or another organic solvent as shown in Figure 4.2.1, the solution was a dark purple and when filtered with Acrodisc 0.2 µm Membrane Syringe Filter (Sigma-Aldrich, USA), it became a waterier golden solution. The yield of the reaction was approximately 61.6%, it is given as approximate because of the filtering process which may have reduced the actual yield.

Additionally, the synthesis of CNDs can create many subproducts which can be considered if they are appropriately eliminated.

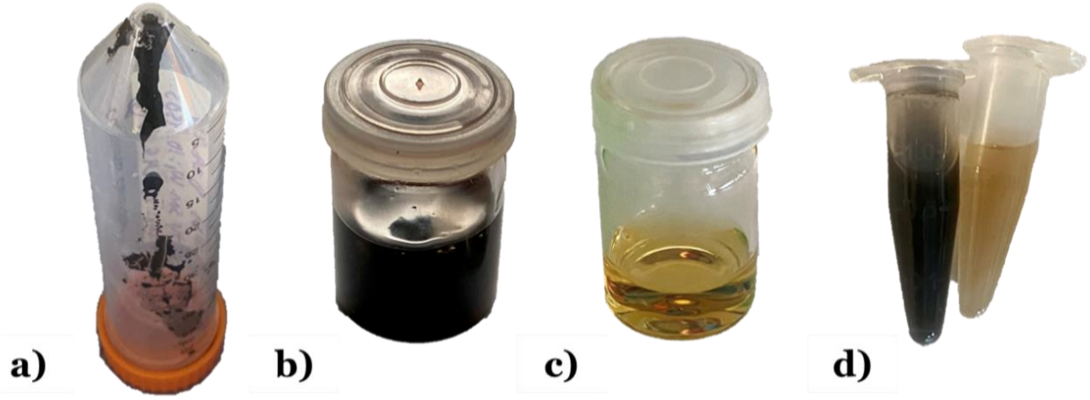

Figure 4.2.1: Carbon nanodots (CNDs) images of a) CNDs after lyophilisation, b) CNDs suspended in ultrapure deionised water in a concentration of 10 mg/mL c) Same suspension as before but after filtration by Acrodisc 0.2 µm Membrane Syringe Filter (Sigma-Aldrich, USA) with a volume loss because of acrodisc filtration and d) comparison in Eppendoff tube of CNDs suspension before and after filtration.

When carbon nanodots (CNDs) are synthesised using citric acid and 1,5-diaminonaphthalene, the process involves heating the precursors (*Figure 4.2.2*), leading to thermal carbonization. This results in the formation of carbon-based nanoparticles with functional groups on the surface, originating from the initial reactants. Citric acid acts as the primary carbon source undergoing decomposition at high temperatures to form the carbon-rich core of the nanodots, while 1,5-diaminonaphthalene introduces nitrogen-containing functional groups that not only modify the surface chemistry but also affect the structural and electronic properties of the nanodots by enabling nitrogen doping within the carbon network. Nitrogen doping can modify the electronic structure of the carbon, introducing new electronic states that enhance properties like conductivity, photoluminescence, and catalytic activity.

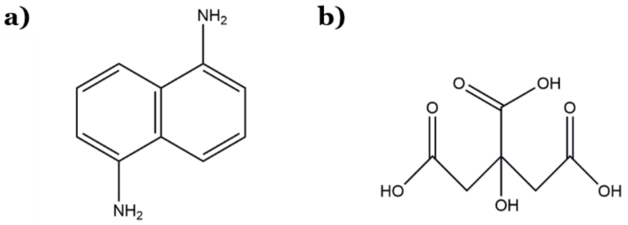

Figure 4.2.2: Carbon nanodots (CNDs) reagent composition chemical structures: a) 1,5-diaminonaphtalene and b) Citric acid. Chemical Structures drawn using ChemDraw® online software.

The surface chemistry of the resulting CNDs is characterized by a variety of functional groups, including amine groups from the 1,5-diaminonaphthalene and carboxyl groups derived from incomplete decomposition of citric acid. These surface groups not only stabilize the nanodots but also provide reactive sites for further chemical modifications, which can be tailored to specific applications. The combination of a carbon core with nitrogen-rich functionalization gives the nanodots improved optical properties, such as enhanced fluorescence, and increased solubility in aqueous environments, making them highly versatile for uses in bioimaging and chemical sensing. Ultimately, the interplay between citric acid's carbon framework and 1,5-diaminonaphthalene's nitrogen-based functional groups leads to the creation of highly tunable carbon nanodots with a broad range of potential applications.

The likely resulting chemical structure is an amorphous or graphitized carbon core, which would be composed mainly of sp^2 carbon networks (similar to graphitized structures) with some sp^3 carbon regions, this arises from the carbonization of citric acid. The possible surface functional groups would be carboxyl groups (-COOH), amine groups ($-NH_2$) and nitrogen doping (N) into the carbon core, forming pyrrole or pyridine-like sites. Furthermore, a possible surface functional structure would include the presence of nitrogen and oxygen atoms on the surface which may generate amine acid-like structures or amide bonds (-CONH).

4.2.2 *Electrospinning: coaxial and single needle, solution preparations and results*

The PHB and PHB/CND solutions shown in *Table 3.1.1* were prepared and electrospun as described in section 3.2 using a rotating drum collector covered in foil. The ambient parameter conditions could not be controlled and oscillated around 18.8-25.6°C and humidity oscillated between 23-73%, which in turn, affected fibre reproducibility.

Three different needle gauges were used to change the size of the resulting fibres. In *Table 4.2.1,* the internal diameters (ID) of each of the selected needle gauge sizes are shown, where 14G is the largest diameter. Additionally, the outer diameter (OD) is considered because the 18G is inside the 14G needle as this is the coaxial needle design creating a smaller cross sectional area than that portrayed when it is an independent needle. When subjected to a high voltage both needles create fibres maintaining a stable Taylor´s cone under stable ambient conditions.

Table 4.2.1: The different needle gauge sizes utilised in the electrospinning experiments. Approximate ID values were obtained from Sigma Aldrich (USA) [2].

Needle Gauge	Nominal Internal diameter (mm)	Nominal Outer diameter (mm)	Cross sectional area (mm^2)
21 (single needle)	0.495	0.813	0.192
18 (coaxial, inner needle)	0.838	1.270	0.552
14 (coaxial, outer needle)	1.600	2.108	2.010 (effectively since it is a coaxial needle)

The resulting fibre meshes created were different shades of white, light pink and dark purple depending on the concentration of CNDs added to the shell solution. As showed in the *Figure 4.2.3 a) to e)*, when no CNDs were added, that is, the only single needle electrospinning, the fibre mesh was white, and then the colour increased until a dark purple was seen with the highest concentration (10%) for the coaxial fibre meshes. The colour shade variations sustain that macroscopically the addition of CNDs on the fibre meshes was accomplished.

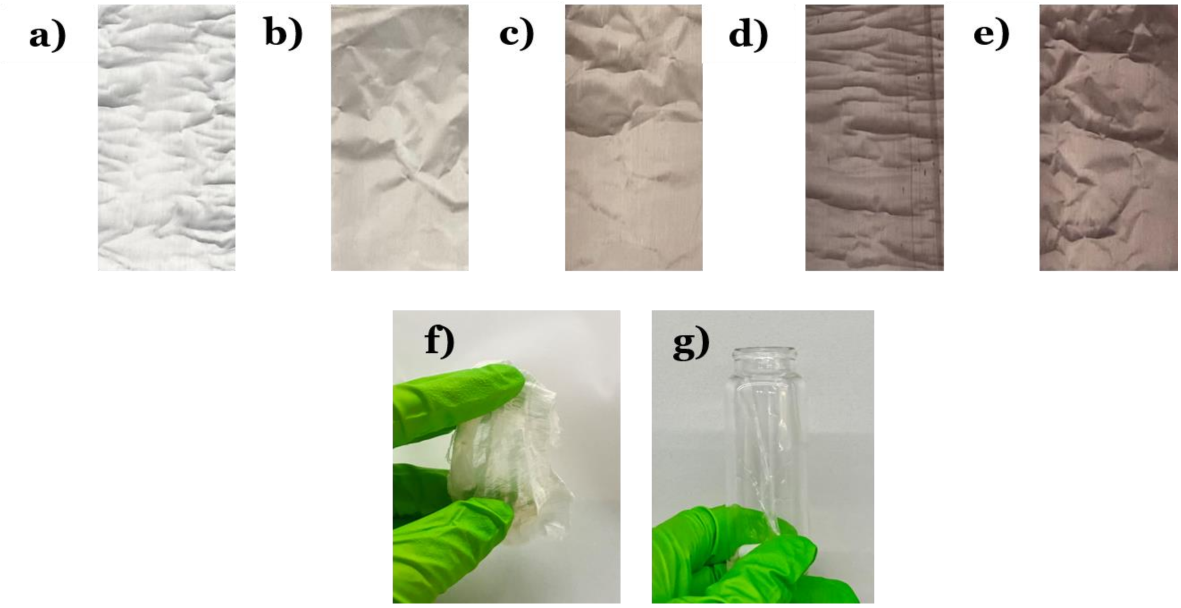

Figure 4.2.3: PHB fibre meshes where different concentrations of CNDs were added and, therefore, it affected macroscopically its colour a) 0% b) 1% c) 2.5% d) 5%, and e) 10% of CNDs were added. f) Nature of the fibres. g) Membrane formed after leaving the PHB solution in room temperature for 2 minutes.

When preparing the PHB solutions and PHB/CND solutions for electrospinning, they had to be kept warm (40-55°C). This was because, after approximately 1 minute at room temperature, the solution would start turning into a membrane-like structure that is difficult to dissolve. After the complete dissolution of the polymer had occurred, the solution was then transferred to a syringe and electrospinning started immediately. It was noticed that the PHB created thicker fibres compared to other commonly used polymers such as polyacrylonitrile (PAN) under the same electrospinning conditions After electrospinning, the fibre meshes had a cottonwool-like nature with a notable resistance to stretching (*Figure 4.2.3 f)*).

4.3 Characterisation: Results and Discussions

4.3.1 *Scanning Electron Microscopy (SEM)*

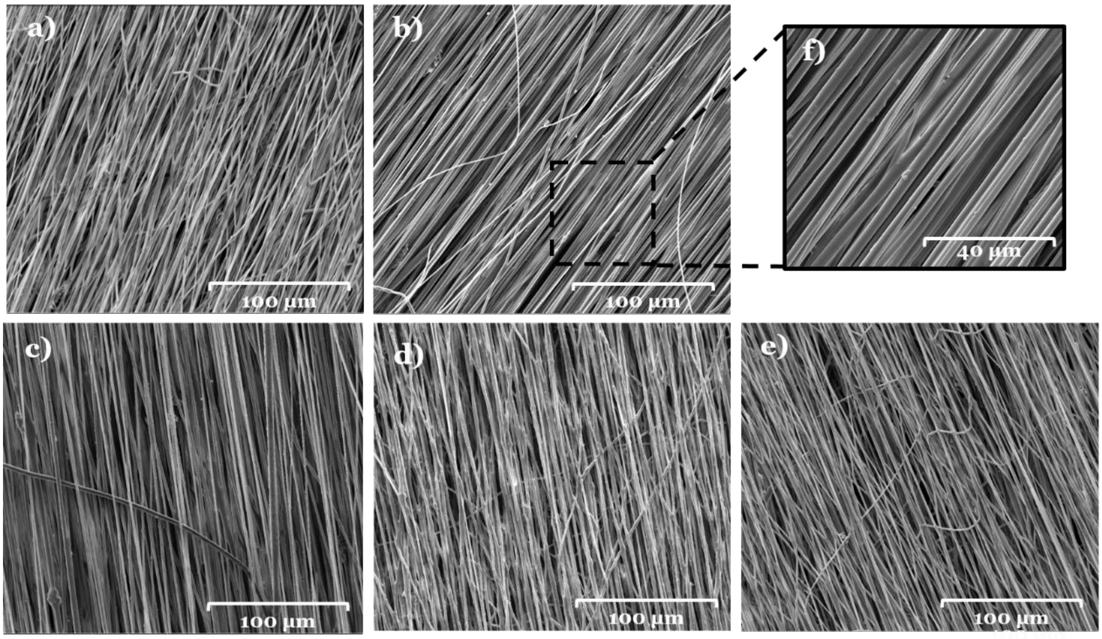

Figure 4.3.1: SEM micrographs used to measure fibre diameter of the PHB fibre meshes a) with 0%, b) 1%, c) 2.5%, d) 5% and e) 10% of added CNDs. These micrographs were captured at a magnification of 1000X. f) Higher magnification on Panel b) at a magnification of 3000X. Scale bars a)-e) 100 μm, f) 40 μm.

During SEM imaging, fibre alignment was relevant. This alignment was produced by the rotating drum collector, which pulls the fibres while they are being formed in the jet stream. The fibre diameter for each of the analysed fibres is listed in *Table 4.3.1*. It can be observed that the fibres became thinner as more carbon nanodots were added; this can be explained by considering that the solutions containing more CNDs have higher viscosity. A viscous electrospinning solution improves fibre formation because, according to literature [34], [74], it reduces solvent evaporation, which allows for better control over the spinning process and helps in maintaining the integrity of the fibres as they are formed. Furthermore, the polymer chains are better aligned and more thoroughly stretched, resulting in stronger and more durable fibres.

Table 4.3.1: Fibre diameter of PHB fibre meshes with the addition of 0%, 1%, 2.5%, 5% and 10%. Fibre diameter were calculated and using ImageJ® software (USA). The diameters of 50 fibres were measured for each type of fibre mesh to determine the average fibre diameter. Table column colours change from white to purple showing the different shades of the fibre meshes.

Sample	Estimated fibre diameter (μm)
PHB fibre mesh with 0% added CNDs	2.29 ± 0.48
PHB fibre mesh with 1% added CNDs	2.18 ± 0.69
PHB fibre mesh with 2.5% added CNDs	1.84 ± 0.76
PHB fibre mesh with 5% added CNDs	1.82 ± 0.70
PHB fibre mesh with 10% added CNDs	1.52 ± 0.44

Energy-dispersive X-ray spectroscopy (EDXS) analysis was chosen for compositional/elemental analysis of the fibre meshes analysed by SEM Microscopy. It was selected to investigate if, when increasing the concentration of carbon nanodots (CNDs) in the meshes, the amount of nitrogen would increase in the sample, thus increasing the polarity of the external layer of the product.

As presented in *Figure 4.3.2*, the EDXS maps showed the presence of nitrogen in the meshes that had CNDs included, with a gradual increase in volume as the concentration grew higher. However, the fibre samples being polymeric are sensitive to high voltage and to a larger aperture than in imaging mode (in order to increase the signal), this rapidly degraded the sample; therefore, the EDXS spectrum was not a reliable source on determining the chemical composition of all the meshes, as they degraded rapidly during EDXS. The scanning time for each sample to obtain sufficient signal was around 5 minutes.

Thus, it was decided to try a more sensitive technique to analyse the surface composition and chemical states of the samples as a result XPS analysis was done.

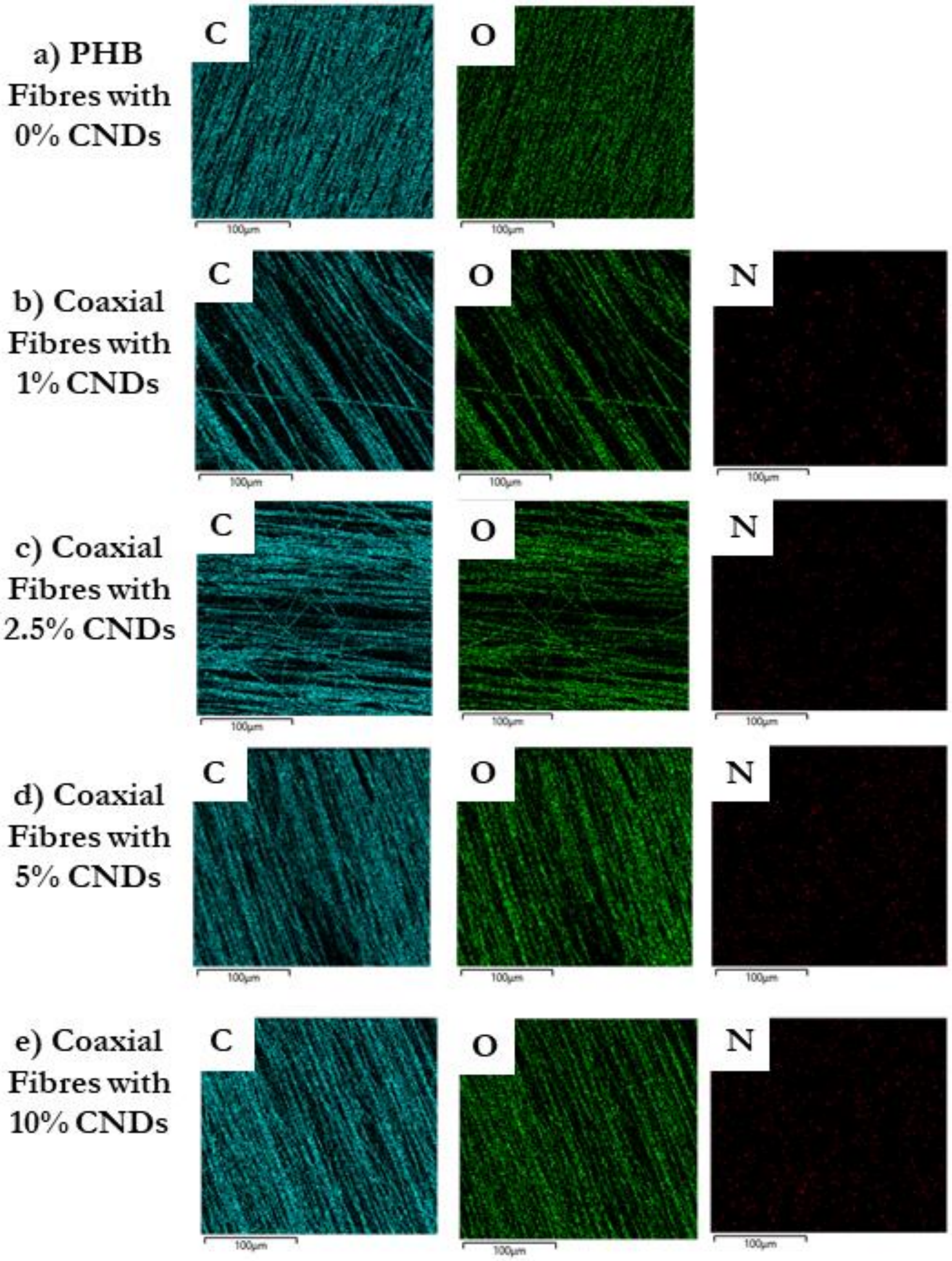

Figure 4.3.2: Energy-dispersive X-ray spectroscopy (EDXS) maps identifying the spatial distributions of C (blue), O (green), and N (red) of a) PHB fibre mesh with 0%, b) 1%, c) 2.5%, d) 5% and e) 10% of added CNDs. These images were captured at a magnification of 1000X. All scale bars are 100 µm.

4.3.2 *Transmission Electron Microscopy (TEM)*

For TEM imaging, *Figure 4.3.3* shows two micrographs where in *Figure 4.3.3 a)* the synthetised CNDs seem to be presenting a turbostratic carbon structure, a distinct type of carbonaceous solid with structural organization that falls between amorphous carbon and crystalline graphite. The amorphous phase is a mixture of sp^2 and sp^3 bonds, it has no long-range crystalline order and typically contains hydrogen and nitrogen in its structure. On the other hand, the graphite phase is made up of carbon atoms bonded in sp^2 hybridization, nonetheless, in the case of turbostratic carbon, unlike in graphite, where the layers stack in a well-ordered fashion, the layers in turbostratic carbon are misaligned and do not stack neatly on top of one another. Instead, they are slightly bent, twisted, or randomly arranged, giving it a more disordered structure while still retaining some graphite-like characteristics [75], [76].

The carbon nanodots displayed a mean diameter of 20.32 ± 5.66 nm. This size is larger than reported in the literature [77] by other groups, but it can be optimised in future work using more dispersive treatments.

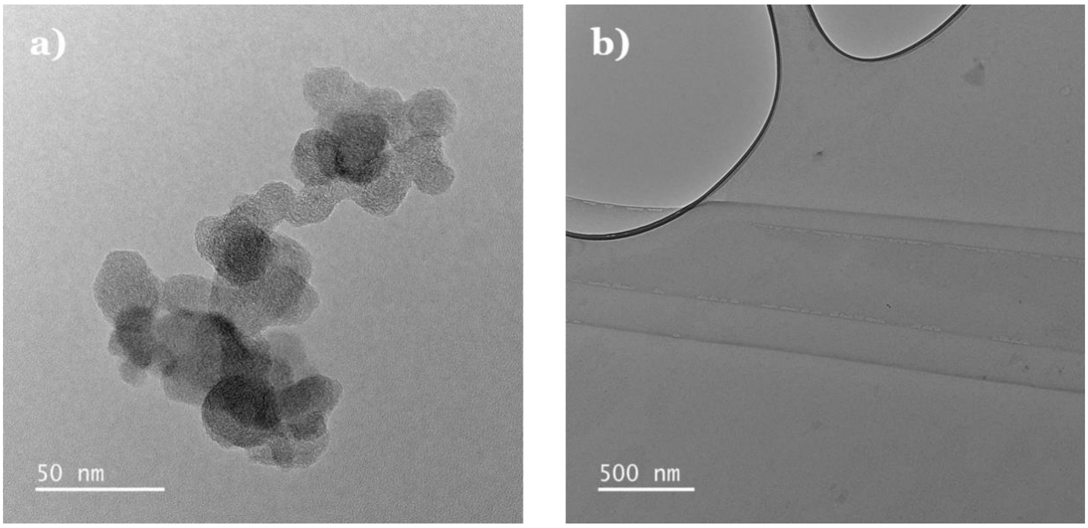

Figure 4.3.3: TEM micrographs of a) CNDs and b) coaxial fibre with 10% CNDs added. Scale bars a) 50nm, b) 500nm.

In *Figure 4.3.3b)*, the core-shell arrangement of the 10% CNDs added electrospun coaxial fibre mesh was noticeable. The TEM images show that the thickness of the shell layer was variable among fibres and thicker in some areas. The core layer was approximately 58.9% of the fibre thickness, where the shell layer varied along the length of the fibre.

4.3.3 *Dynamic Light Scattering (DLS)*

To determine the average hydrodynamic diameter of the CNDs, Dynamic Light Scattering (DLS) was used, as it is a widely recognised method for analysing the size distribution of nanoparticles in suspension, providing accurate insights into their behaviour and potential aggregation in solution. However, this technique does not provide information about the quantity of particles or their scattering efficiency, σ [78]. Additionally, the formation of large aggregates cannot be entirely ruled out, as the CNDs, though initially well dispersed in water and yet filtered to minimise agglomerates, were observed to slowly agglomerate and settle to the bottom after a few minutes. To re-disperse them for analysis, they had to be subjected to an ultrasonic bath again.

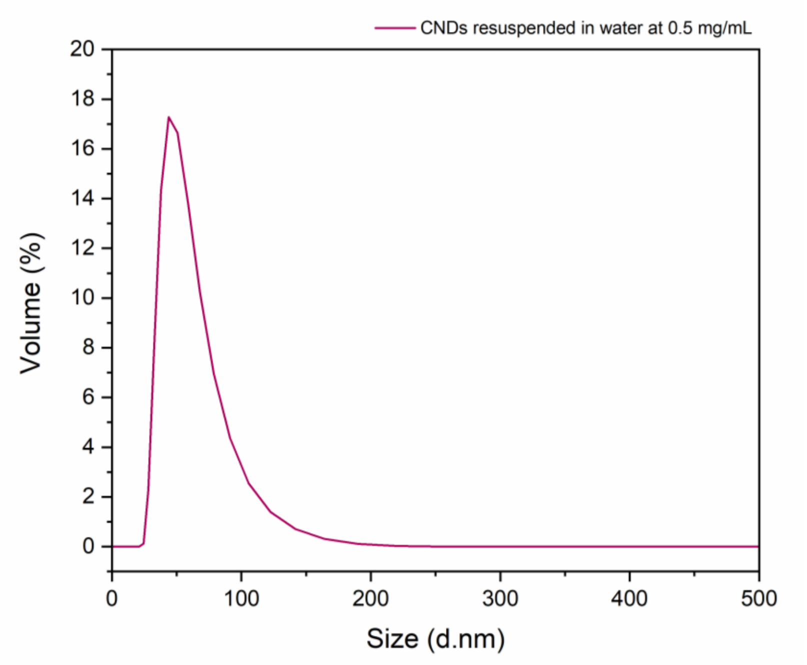

Figure 4.3.4: Average hydrodynamic size diameter of carbon nanodots suspended in water at 0.5 mg/mL obtained by DLS.

The average hydrodynamic particle size was determined to be 57.76 nm in volume with a standard deviation of 26.27 nm (*Figure 4.3.4*). The carbon nanodots showed a unimodal distribution in size with a Polydispersity Index (PDI) of 0.18, suggesting that is a uniform sample size.

4.3.4 *ATR-FTIR Spectroscopy*

FTIR showed small changes in the chemical structure of PHB after being subjected to electrospinning. This indicates that the chloroform used to dissolve the solution was completely evaporated. Characteristic peaks of the PHB fibre meshes with 0%, 1%, 2.5%, 5% and 10% of added CNDs are: at 2976 cm^{-1} corresponding to the aliphatic C-H bonds corresponding to the backbone of the polymer; a very strong band at 1720 cm^{-1} due to the stretching vibrations of the carbonyl C=O bonds in the esters; and finally, a band for the stretching vibrations of the C-O present in the esters at 1261 cm^{-1}. While the characteristic peaks for the CNDs are a band for the stretching vibrations of the N-H from the presence of amines at 3390 cm^{-1}; a band at 3232 cm^{-1} associated with aromatic ring vibrations; a band at 2982 cm^{-1} corresponding to aliphatic C-H bonds on the surface of the CNDs chemical structure; a very strong band at 1716 cm^{-1} representing the carbonyl stretching vibration of the C=O bonds in the carboxylic acid groups added by the incorporation of citric acid; an intermediate intensity band at 1628 cm^{-1} showing the stretching of the C=C double bond in an alkene; a broad band at 1182 cm^{-1} due to the stretching vibration of the C-N bond of amines; and finally, a band for the stretching vibration of C-O the carboxyl acids at 1023 cm^{-1} (*Figure 4.3.5*) [79].

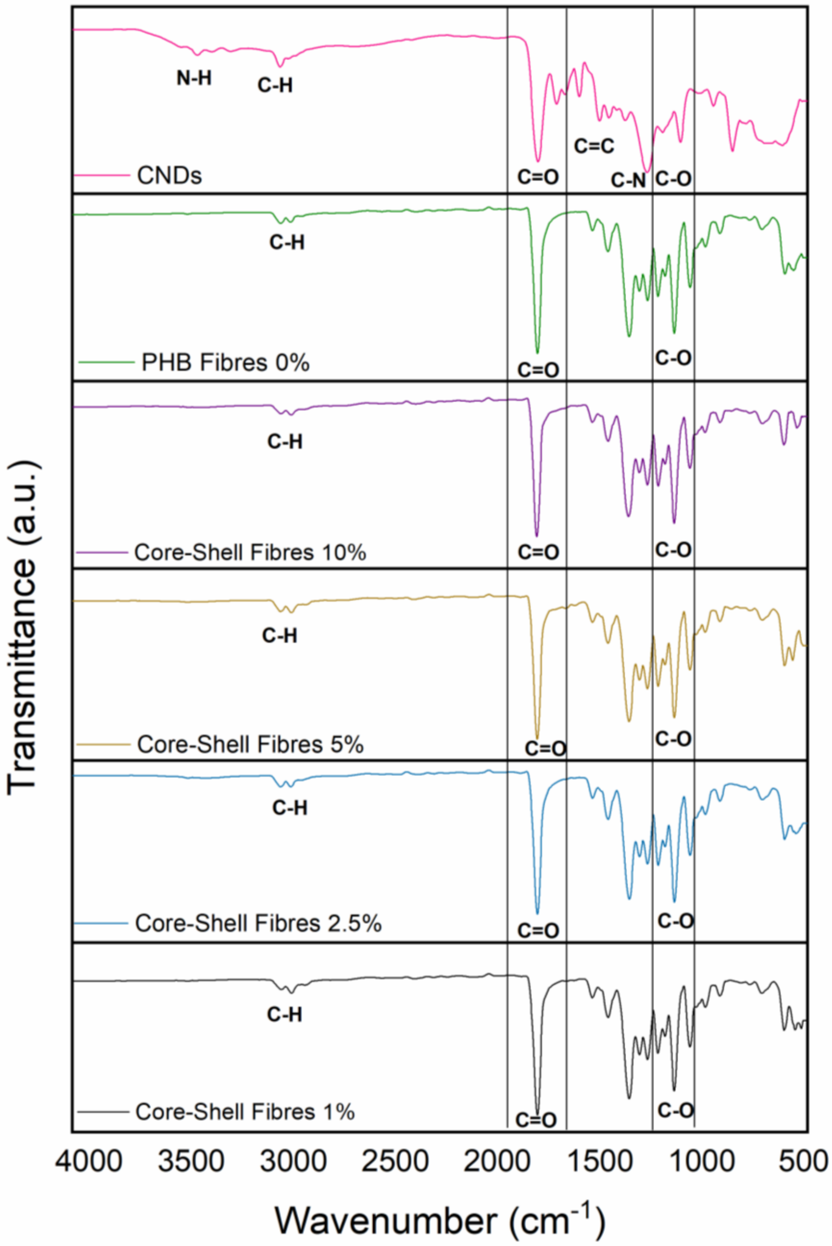

Figure 4.3.5: Stacked FTIR Spectra of synthetised CNDs, PHB fibre meshes with 0%, 1%, 2.5%, 5% and 10% of added CNDs.

The addition of CNDs into the different fibre meshes has been shown to not be detectable by the ATR-FTIR; this is because there is only a very small percentage of the characteristic CNDs functional groups that are added into the whole fibre mesh. Even though it is a coaxial fibre mesh, most of the fibre mesh is the PHB polymer, demonstrating this on the ATR-FTIR Spectra. Techniques that are more sensitive can be used to detect the incorporation of the carbon nanodots in the structure.

4.3.5 *UV-Vis Spectroscopy*

The CNDs solution at 5x10^{-5} nm in water presents two absorption bands at 230 and 316 nm in the UV–vis absorption (*Figure 4.3.6*). In UV-Vis spectroscopy, different chromophores absorb light at specific wavelengths, corresponding to their electronic transitions. In the case of the synthesised CNDs, the reagents utilised to their production are 1,5-diaminonaphtalene (1,5-DAN) and citric acid. 1,5-DAN has an aromatic naphthalene ring with amino groups, which are key functional groups for this absorption bands.

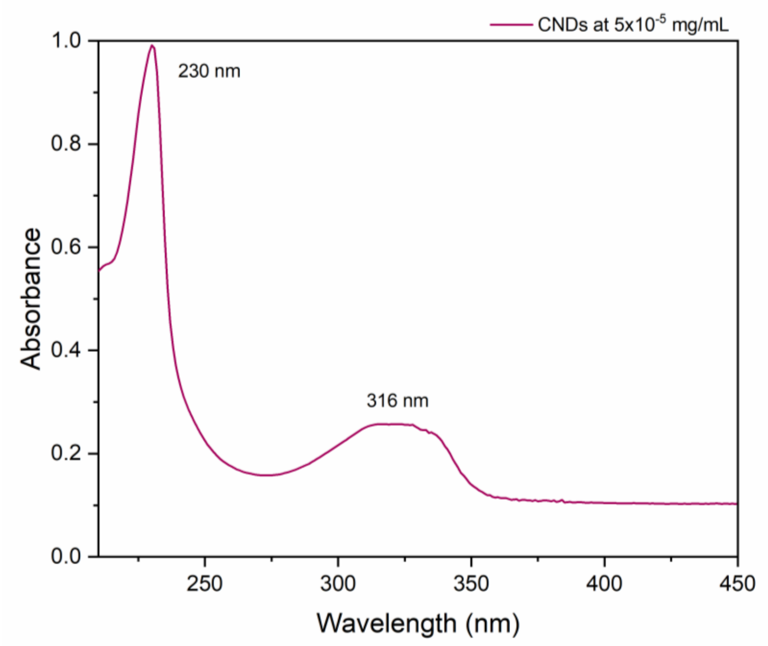

Figure 4.3.6: UV-Vis Absorption Spectrum of the CNDs displaying a bimodal distribution at with an absorption peak at 230 nm and 316 nm.

The absorption at 230 nm is likely due to the π to π* transitions of the aromatic naphthalene ring. Aromatic rings typically absorb in this range because of their conjugated π-electron systems [80] . At 316 nm, the absorption could be related to the extended conjugation involving the naphthalene ring, potentially with interactions involving the amino groups. The extended π-system of naphthalene and its derivatives can show absorption in this range. Citric acid generally absorbs at higher wavelengths due to the presence of carboxyl groups, but in combination with 1,5-DAN, any absorption of this molecule would be around 316 nm. This specific absorption might be influenced by the interactions between the naphthalene and citric acid components in the CNDs, reflecting extended conjugation or specific interactions between the two substances.

4.3.6 *Fluorescence Spectroscopy*

To investigate the optical properties of the carbon nanodots (CNDs) in water, a highly diluted solution ($1x10^{-12}$ mg/mL) was prepared. Fluorescence spectra was obtained from this solution to determine if both UV and visible light could activate the CNDs. Visible light irradiation is preferred for hernia repair applications, as it offers a safer and more versatile approach for clinical use, making it more suitable for human patient exposure. However, due to the inherent properties of the CNDs, the solution exhibited such intense fluorescence that it exceeded the detection limits of the equipment. A lower concentration solution was made to reduce this problem, but the CNDs seemed to be more affected by the light emission above $1x10^{-13}$ mg/mL, were they appeared to be degrading, giving a broader and irregular peak as the solution was more diluted. Therefore, the initial concentration was selected, to display the resulting bands that correspond to the sample.

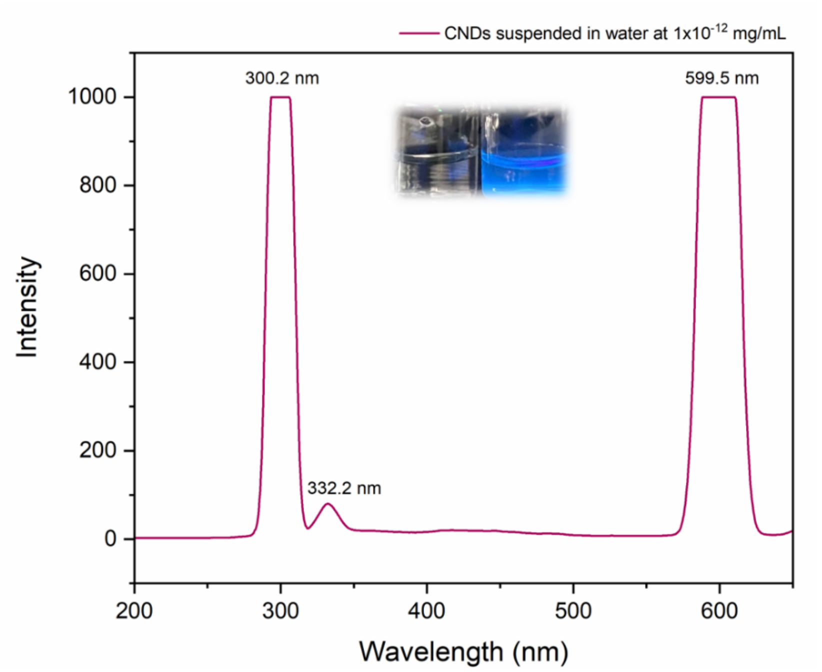

Figure 4.3.7: Fluorescence Spectrum of the CNDs with emission peaks at 300.2 nm, 332.2 nm and 599.5 nm.

The obtained fluorescence spectrum with emission peaks at 300.2 nm, 332.2 and 599.5 nm in *Figure 4.3.7*, generated with an excitation wavelength of 300 nm, can be explained as follows [80]:

- **300.2 nm:** This peak is too close to the excitation wavelength, which could be attributed to Rayleigh scattering; that is elastic scattering where the emitted light is at the same wavelength as the excitation light. But since it is a very strong peak, another less likely possibility is that it is due to absorption of the emitted light, where the molecules in the CNDs would absorb some of the emitted photons and re-emit them at nearly the same wavelength.

- **332.2 nm:** For this peak, since CNDs have naphthalene rings in their chemical structure originating from 1,5-DAN, it is likely due to a transition from an excited state of the aromatic system back to the ground state, since aromatic compounds often exhibit fluorescence in the UV range.
- **599.5 nm:** This emission might indicate a more complex behaviour, such as interactions between the molecules in the solution, like charge transfer between 1,5-DAN and citric acid or a secondary emission process, which might involve another part of the molecule. The visible peak at 599.5 nm, which falls in the orange-red range, suggests a greater energy loss from excitation to emission. This could be due to factors such as extended conjugation in the molecule or interactions with other components in the solution.

Since the application is to activate the material with visible light for biomedical applications, the emission at 599.5 nm is particularly important. This emission in the visible range suggests that the material could be responsive or active when irradiated with visible light, making it potentially useful for applications such as hernia repair, where visible light can safely penetrate skin and the underlying soft tissue to reach the hernia repair implant site without causing harm.

4.3.7 *Contact Angle Measurement of Sessile Drops/Drop Shape Analysis*

Contact angle measurement analysis was performed to examine the solid surface properties and wettability of the PHB fibre meshes with different added concentrations of CNDs and compared to the CNDs alone (*Figure 4.3.8)*.

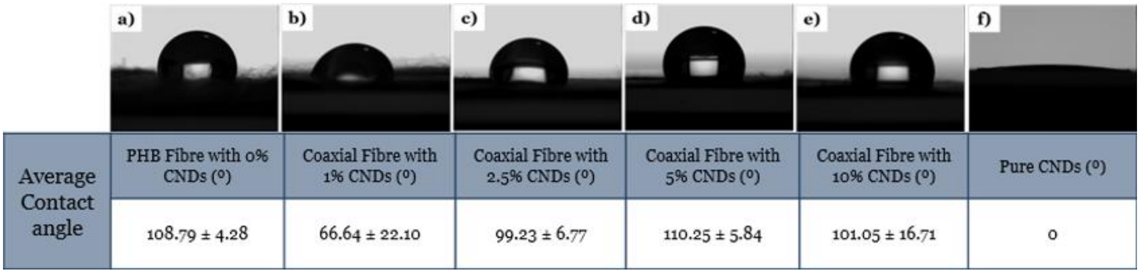

	PHB Fibre with 0% CNDs (°)	Coaxial Fibre with 1% CNDs (°)	Coaxial Fibre with 2.5% CNDs (°)	Coaxial Fibre with 5% CNDs (°)	Coaxial Fibre with 10% CNDs (°)	Pure CNDs (°)
Average Contact angle	108.79 ± 4.28	66.64 ± 22.10	99.23 ± 6.77	110.25 ± 5.84	101.05 ± 16.71	0

Figure 4.3.8: Contact angle measurements of a) PHB Fibre with 0% CNDs, b) coaxial fibre with 1% of added CNDs, c) coaxial fibre with 2.5% of added CNDs, d) coaxial fibre with 5% of added CNDs, e) coaxial fibre with 10% of added CNDs and e) synthesised CNDs.

According to literature, a surface with a contact angle more than 90° is considered hydrophobic, a contact angle below 90° hydrophilic and a contact angle of 0° is considered to have ideal wetting or spreading [81]. The synthesised CNDs presented a contact angle approaching 0º which indicates a high surface energy. The different PHB fibre meshes displayed a contact angle higher than 90º except for the coaxial PHB fibre mesh with the addition of 1% CNDs. This mesh appears to be displaying hydrophilic behaviour, providing a higher surface energy compared to the other fibres.

The fibres analysed have are synthetised from long-chain hydrocarbons, which contributes their hydrophobic nature. This chemical structure minimizes interactions with polar water molecules. Furthermore, these long chains have polar groups like carbonyl groups coming from the ester structure. Subsequently, the hydrophilic fibre mesh could have had a better arrangement of these polar groups from the shell solution while being electrospun and, in consequence, is more hydrophilic in comparison.

4.3.8 *Thermogravimetric analysis (TGA)*

Figure 4.3.9 displays the thermogravimetric analysis of PHB fibre meshes with the addition of 0%, 1%, 2.5%, 5% and 10% compared to the pure synthetised CNDs. It should be noted that in the *Table 4.3.2* and the residue percentage presented in weight (%).

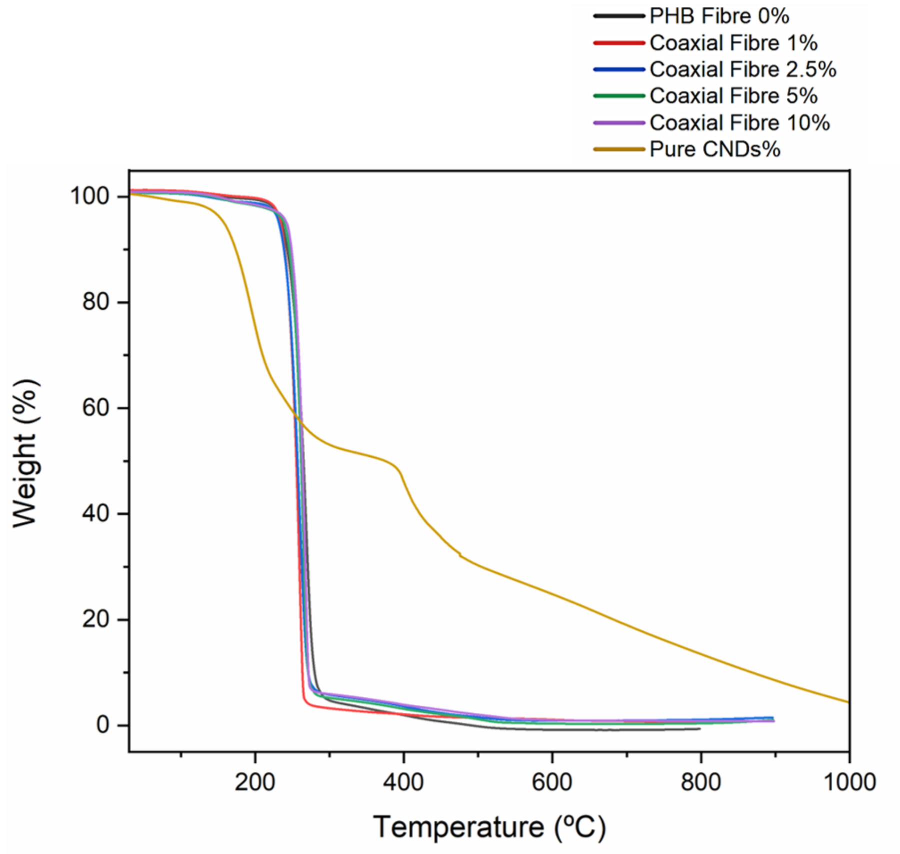

Figure 4.3.9: Representative TGA curves of PHB fibre meshes with the addition of 0%, 1%, 2.5%, 5% and 10% compared to the synthetised CNDs alone.

Table 4.3.2: Thermal properties of PHB fibre meshes with the addition of 0%, 1%, 2.5%, 5% and 10% compared to the synthetised CNDs alone.

Sample	T_{onset} (ºC)	T_d (ºC)	Residue (%)
PHB fibre mesh with 0% added CNDs	232.84	767.73	-0.793
PHB fibre mesh with 1% added CNDs	230.12	773.33	0.66
PHB fibre mesh with 2.5% added CNDs	242.97	762.28	0.69
PHB fibre mesh with 5% added CNDs	241.16	781.73	0.33
PHB fibre mesh with 10% added CNDs	243.53	787.44	0.87
Synthesised CNDs	92.77 & 401.77	973.80	5.74

In *Table 4.3.2*, the thermal degradation of the PHB fibre meshes in a nitrogen atmosphere occurs above 230 °C and as a higher concentration of CNDs, a higher temperature is needed to reach the onset temperature and start the degradation process. The mesh without carbon nanodots added was used as a control and needs a lower temperature to degrade; hence, the residue was under 0%, which can be classified as machine error. The synthetised CNDs had two degradation curves, where the first one is the elimination of residual water, and the second one is where the degradation begins. The equipment had a 1000ºC limitation; according to the data collected another machine that could operate at higher temperatures, would be needed to reach complete degradation of the CNDs.

4.3.9 *Differential scanning calorimetry (DSC)*

Figure 4.3.10 displays the DSC analysis of PHB fibre meshes with the addition of 0%, 1%, 2.5%, 5% and 10% compared to the pure synthetised CNDs. As it is displayed, the fibre meshes showed relatively similar behaviour while the CNDs display a melting point (onset) at a lower temperature. The important parameters to analyse for each sample are shown in *Table 4.3.3* It must be noted that the equipment utilised could not handle degraded or broken samples, therefore, the maximum temperature was the temperature just before the degradation process occurs (onset temperature on TGA).

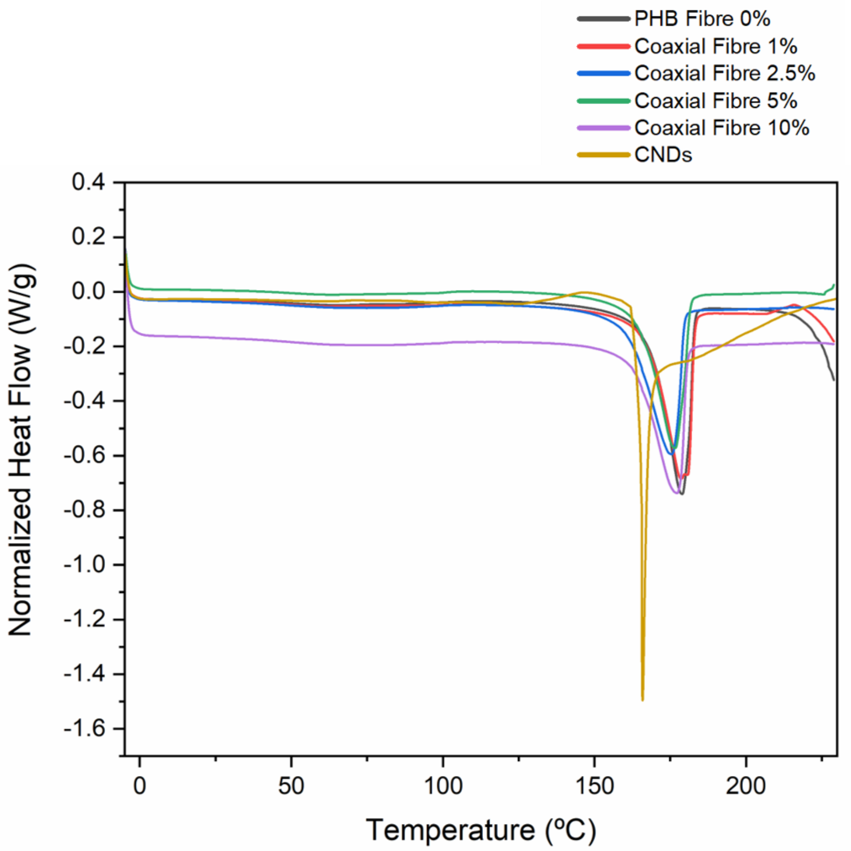

Figure 4.3.10: Representative DSC curves of PHB fibre meshes with the addition of 0%, 1%, 2.5%, 5% and 10% compared to the pure synthetised CNDs.

Table 4.3.3: Calorimetric properties of PHB fibre meshes with the addition of 0%, 1%, 2.5%, 5% and 10% compared to the pure synthetised CNDs.

Sample	Glass Transition Temperature (T_g) (Midpoint, °C)	Melting Temperature ™ (°C)	Enthalpy of Fusion (ΔH_f) (J/g)	% Crystallised
PHB fibre mesh with 0% added CNDs	147.01	182.52	88.74	30.91
PHB fibre mesh with 1% added CNDs	150.66	182.99	83.86	29.21
PHB fibre mesh with 2.5% added CNDs	150.30	179.60	86.63	30.17
PHB fibre mesh with 5% added CNDs	184.20	181.53	84.11	29.29
PHB fibre mesh with 10% added CNDs	147.96	180.27	81.02	28.22
Synthesised CNDs	162.84	165.54	50.38	17.55

The selected parameters for evaluation are:

- **Glass Transition Temperature (T_g)**, which is a crucial parameter that indicates the temperature at which a polymer changes from a glassy to a rubbery state, significantly affecting its mechanical properties and usability [82].
- **The Melting Temperature (T_m)** is vital for semi-crystalline or crystalline polymers, marking the point where the material changes from solid to liquid, which is essential for processing and application conditions [82].
- **Enthalpy of Fusion (ΔH_f)** provides insight into the heat required for melting, which is related to the'polymer's degree of crystallinity and can influence its performance characteristics [82].
- **% Crystallised**: The percentage of crystallinity in a polymer significantly influences its thermal and mechanical properties. Higher crystallinity generally leads to increased mechanical strength and stiffness, as the crystalline regions provide structural integrity, while amorphous regions contribute flexibility. Additionally, the degree of crystallinity affects thermal behaviour, with more crystalline polymers typically exhibiting higher melting temperatures and greater thermal stability [82].

Together, these parameters are critical for understanding the thermal behaviour and suitability of polymers. When considering the results, we must understand that the PHB fibre meshes melt at around 181-184°C suggesting that the polymer is likely semi-crystalline, as amorphous polymers do not have a defined melting point. Semi-crystalline polymers typically exhibit both crystalline and amorphous regions, resulting in a melting temperature where the crystalline portions transition to a liquid state. Additionally, observing the % crystallised we can see that the fibres as well as the CNDs are semi-crystalline, furthermore justifying that the carbon nanodots have a turbostratic carbon structure.

4.3.10 *X-ray photoelectron spectroscopy (XPS) Analysis*

XPS analysis was conducted on PHB fibre mesh with 0% added CNDs and the synthesised CNDs as controls, alongside coaxial fibre meshes containing 2.5% and 10% added CNDs. To examine the chemical composition and surface structure of each sample, X-ray Photoelectron Spectroscopy (XPS) was performed, with the data analysed using Avantage® software. Each spectrum was charge-corrected to the dominant C 1s peak at 284.81 eV, corresponding to adventitious carbon. To assess sample uniformity, spectra were collected from three different locations on each sample [83], [84].

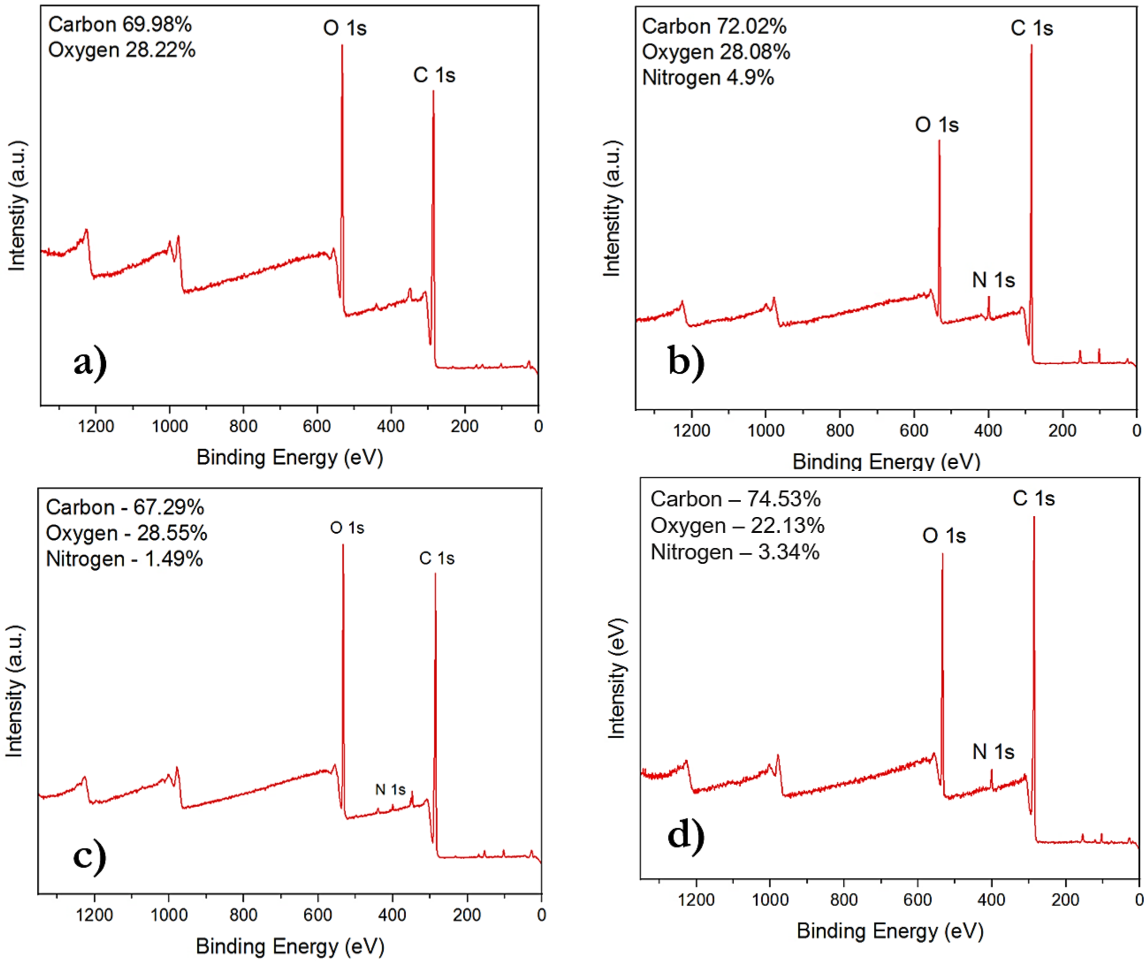

Figure 4.3.11: XPS Spectra of a) PHB fibre mesh with 0% CNDs, b) synthesised CNDs, c) coaxial fibre mesh with 2.5% added CNDs and d) coaxial fibre mesh with 10% added CNDs.

The XPS spectra in *Figure 4.3.11 a*), showed the characteristic elements of a PHB fibre, with a C 1s peak at 286 eV and O 1s peak at 532 eV. In *Figure 4.3.11 b)*, the characteristic peaks for the synthetised CNDs can be observed, with a C 1s peak at 286 eV, O 1s peak at 533 eV and a N 1s peak at 400 eV. These samples were kept as a control to be able to analyse the coaxial fibres and how the addition of the CNDs may affect in their carbon, oxygen and nitrogen percentage.

Figure 4.3.11 c) and d), shows the peaks of a PHB fibre mesh with 2.5% added CNDs and a PHB fibre mesh with the addition of 10% CNDs, with a C 1s peak at 287 eV, O 1s peak at 532 eV and a N 1s peak at 400 eV. Both samples showed that after the addition of CNDs in the electrospinning solution, even in different concentrations, nitrogen is seen on the surface layer of the sample (atomic percentage of nitrogen).

To explain the previous spectra, we must mention that in the case of carbon, most relevant peak was at around 286 and 287 eV, most likely related to the presence of C-O and C=O bonds, being in the case for all the samples. In the case of the CNDs, the citric acid when decomposed provides the C-O and C=O groups to the sample and for the fibre meshes, the PHB molecule and therefore, the fibres are a polyester. In the case of oxygen, the most prevalent peak was around 533 eV signifying the carbonyl groups previously mentioned, C=O. In the case of nitrogen, in the PHB mesh without the addition of CNDs an N 1s peak, is not seen but the in the other samples it is present. When comparing the peaks, the characteristic peak at 400 eV from the CNDs, which can be interpreted as a C-N peak, can be observed in the surface layer of the coaxial fibres. The CNDs by themselves do not contain much nitrogen when compared to carbon and oxygen, this is probably due to the carbonisation process it went through and how the structure was formed. Nevertheless, even on the sample with 2.5% added CNDs, nitrogen is observable, increasing as the concentration increases. The presence of nitrogen in the surface layer of the coaxial fibres increased the polarity of the outer-most layer of the fibres. The percentages are listed in the *Table 4.3.4*.

Table 4.3.4: XPS element percentages of the PHB fibre meshes and the synthesised CNDs as shown in *Figure 4.3.11*.

Sample	Carbon (%)	Oxygen (%)	Nitrogen (%)
PHB fibre mesh with 0% added CNDs	69.98	28.22	0.00
Synthetised CNDs	72.02	28.08	4.90
PHB fibre mesh with 2.5% added CNDs	67.29	28.55	1.49
PHB fibre mesh with 10% added CNDs	74.53	22.13	3.34

4.3.11 *MTT Assay using L-929 cell line*

The samples were weighed and stored in sterile plastic vials (*Figure 4.3.12*). Triplicate sets were prepared for each of the four testing groups: 24D, 72D, 24C, and 72C, as previously described in *subsection 3.3.11.2 (Mesh Wetting)*. PHB fibre meshes containing 0%, 1%, 2.5%, 5%, and 10% CNDs were tested, with the fibre mesh without CNDs serving as a control to assess whether the inclusion of CNDs induces cytotoxic effects on the final product.

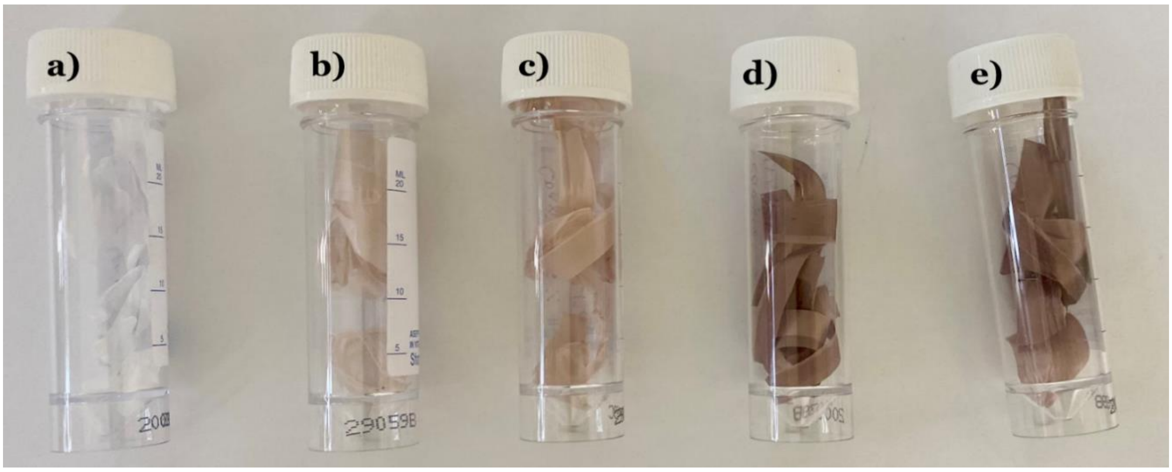

Figure 4.3.12: PHB fibre meshes collected for MTT Assay. PHB fibres with a) 0%, b) 1%, c) 2.5%, d) 5% and e) 10% added CNDs.

After the meshes removal from the aluminium foil covering the rotating drum collector, the fibre meshes exhibited strong electrostatic behaviour, as they resisted detachment from metal tools and other metal surfaces. Since the meshes were created using electrospinning, they were subjected to electric fields, which could have charges the fibres. This made them particularly difficult to manoeuvre during the disinfecting and wetting process (*Figure 4.3.13*), as they needed to be placed in individual well plates using metal tweezers.

During the sterilisation process, fibres containing CNDs tinted the ethanol solution in varying shades of purple. Wells with meshes containing lower CNDs content were lighter, while those with 10% added CNDs produced the darkest purple. This behaviour is likely a release of the CNDs into the organic solution, as they are highly hydrophilic. However, not all CNDs appeared to dissolve; once the ethanol evaporated, macroscopically the fibres retained their characteristic colour. It seems that only the CNDs in the outermost layer of the mesh were released into the solution.

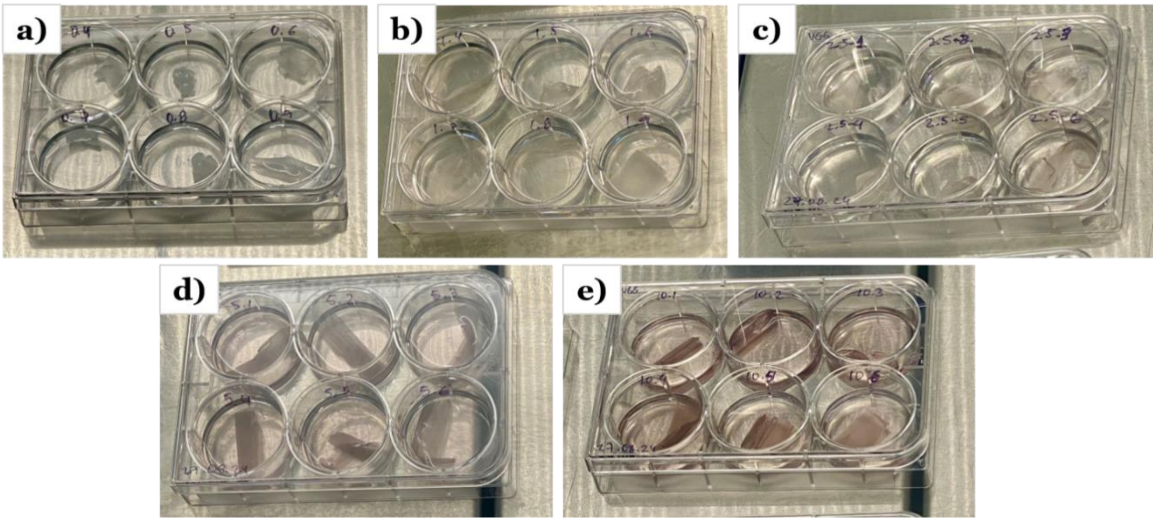

Figure 4.3.13: PHB fibre meshes subjected to disinfection with 70% v/v ethanol for MTT Assay in 6-well plates. PHB fibres with a) 0%, b) 1%, c) 2.5%, d) 5% and e) 10% added CNDs.

During the wetting process, the fibres seemed to resist full immersion remaining near the surface of the media solution. This behaviour could be attributed to the hydrophobicity of the meshes, as they possess a lower surface tension compared to the media solution; therefore, they tend to float. Additionally, the intricate physical structure and texture of the polymer fibre mesh may further inhibit liquid penetration.

After the MTT Assay was performed (*Figure 4.3.14*), cell viability was calculated using the formula previously described in subsection *3.3.11.3 (MTT Assay Procedure after sample conditioning)*. Even after 48 hours of cell growth and a confluence of around 80-90% on all wells, the positive control as well as some wells containing cells subjected to the test media, presented a yellow colour, which represents cell death when interpreted according to the interpretation of the MTT Assay. From the wells that displayed a higher intensity of purple colour they contained test media representing cell proliferation. Therefore, this was investigated under the microscope to see why the positive controls appeared as dead cells, and after the visualisation under the microscope, it was noticed that there were cells present but it they was not as confluent as those wells that are purple. Therefore, at first sight you one cannot tell cell death. This could be due the use an old MTT Reagent and Solvent.

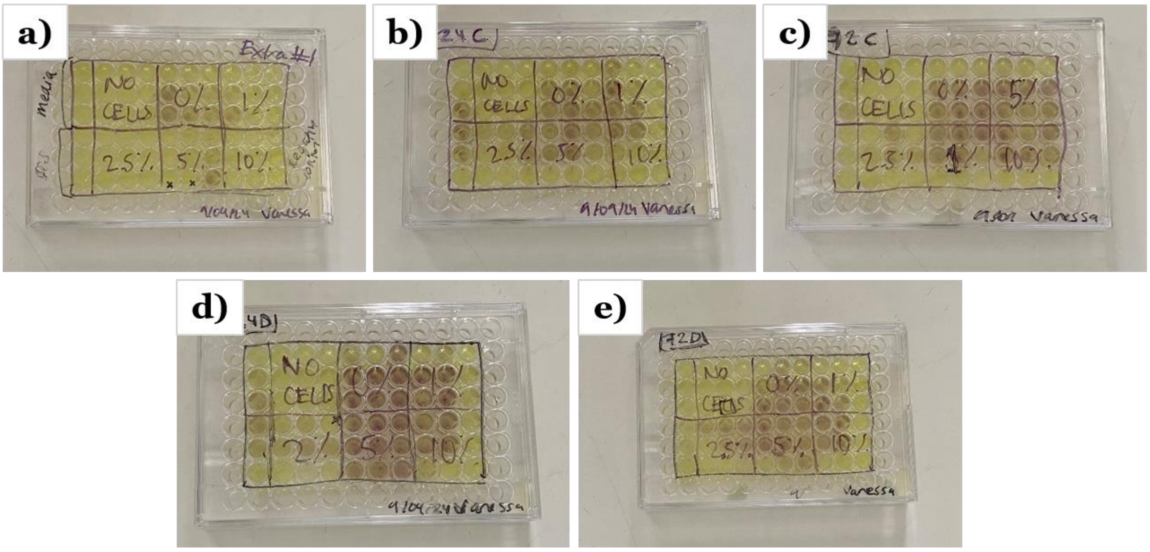

Figure 4.3.14: 96-well plates containing the cells subjected to the MTT Assay after reading the results on the SPECTROstar Nano plate reader (BMG LABTECH, Germany). a) positive control plate, b) 24C plate, c) 72C plate, d) 24D plate and e) 72D plate.

A One-way ANOVA followed by a post-hoc Tukey test was conducted to analyse the MTT results for the 24D, 72D, 24C, and 72C groups. These groups represent different incubation conditions for L929 cells. The 24D group consists of L929 cells incubated for 24 hours with the test media alone (*Figure 4.3.15 a*)), while the 72D group consists of cells incubated for 72 hours with the test media alone (*Figure 4.3.15 b*)). For the 24C group, L929 cells were incubated for 24 hours with the test media, after which the media was aspirated and replaced with fresh media, followed by an additional 24-hour incubation (*Figure 4.3.15 c)).* Finally, the 72C group involved L929 cells incubated for 72 hours with the test media, followed by aspiration and replacement with fresh media, and an additional 72-hour incubation (*Figure 4.3.15 d)).* The C subgroup was designed to test whether residual chloroform in the fibre meshes could affect cell viability, which is important for determining whether any pre-treatment is necessary before potential clinical applications.

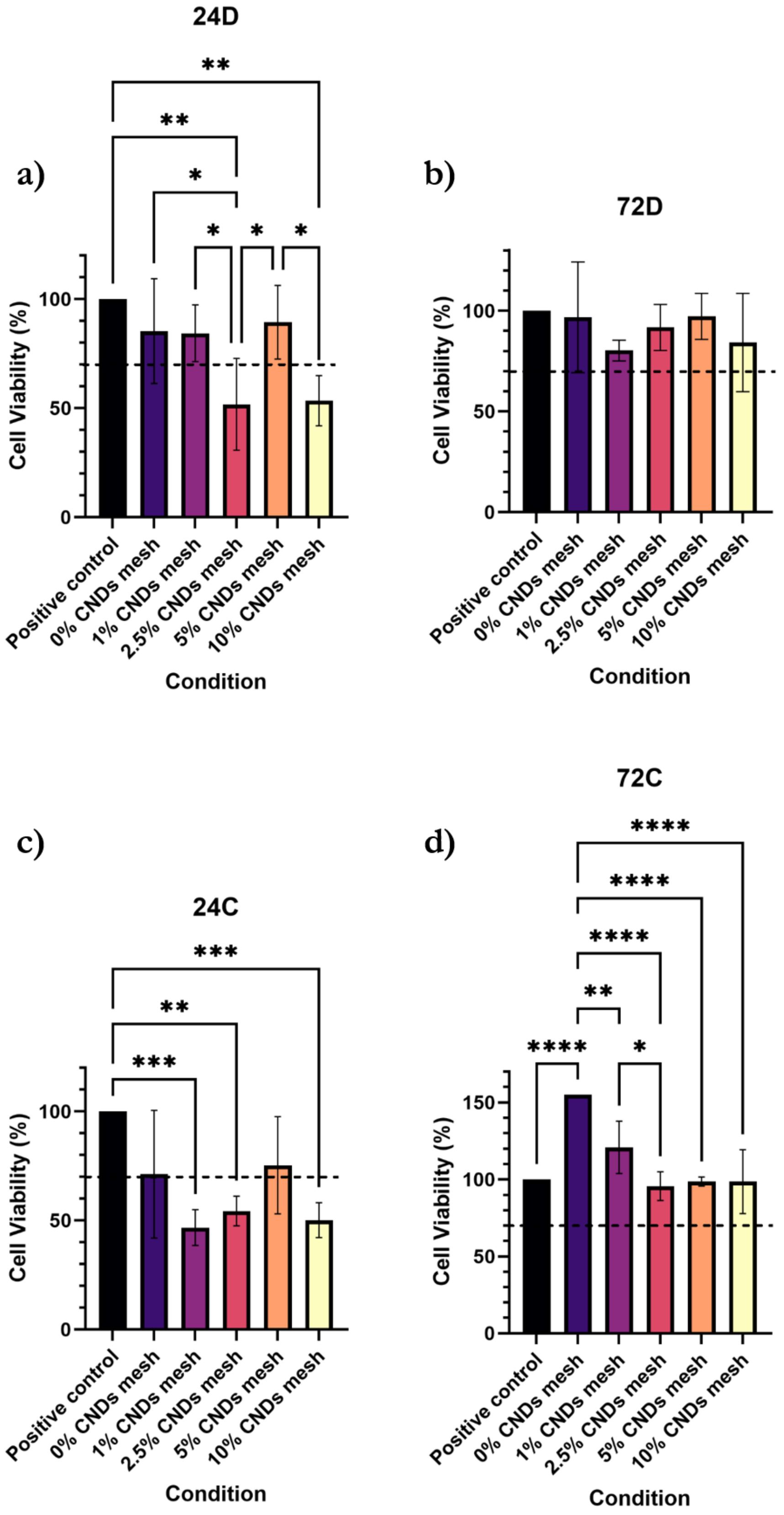

Figure 4.3.15: MTT Assay Results, a) 24C plate, b) 72C plate, c) 24C plate and d) 72D plate results. *p<0.05, ** p<0.01, *** p<0.001, **** p<0.0001. Dotted line indicates 70% limit for cytotoxicity. Graphs were generated using GraphPad® Prism Software.

According to the ISO 10993, Part 5, Annex C: MTT cytotoxicity test [39], in 24D testing group, the meshes with 2.5% and 10% added CNDs are considered cytotoxic, as their cell viability results were below the 70% threshold, at 51.8% and 53.4%, respectively. In contrast, the meshes with 0%, 1%, and 5% added CNDs showed no cytotoxic effect, with all samples demonstrating cell viability above 80% (85.4%, 84.4%, and 89.4%, respectively).

It can be observed that the two meshes are significantly different from the positive control (100%), with a p-value of < 0.01. However, when comparing the meshes between each other as in, 1% of added CNDs to 2.5%, 1% to 2.5%, 2.5% to 5% and 5% to 10% shows that all the differences are statistically significant ($p < 0.05$); which means there is less than a 5% chance that the differences in the data occurred by random chance.

In *Figure 4.3.15 b),* the 72D group is analysed. It is evident that all the meshes are cytocompatible, as they exhibit cell viability above 70%, with no significant differences between them. In *Figure 4.3.15 c),* the results show that the meshes with 2.5% and 10% added CNDs (displaying 54.3% and 50.2% cell viability, respectively) are once again considered cytotoxic in the 24-hour incubation group, in this case the 24C group. Additionally, the mesh with 1% CNDs, compared to the 24D group, is also deemed cytotoxic, exhibiting even greater cytotoxicity than the other two meshes, with a cell viability of 46.8%. Simultaneously, the 0% and 5% are deemed cytocompatible with 71.3% and 75.4% cell viabilities exhibited. In the 24D group, we can find a statistical significance ($p < 0.01$) between the positive control and the 2.5% added CNDs mesh. Additionally, we can find a highly significant difference ($p < 0.001$) when comparing the positive control and the 1% added CNDs mesh and when comparing the positive control with the 10% added CNDs mesh.

In *Figure 4.3.15 d),* it is evident that all the meshes can be classified as cytocompatible, as they demonstrate cell viability greater than 70%. Notably, the control mesh (0% added CNDs) and the mesh with 1% added CNDs exhibit increased performance, with cell viabilities of 154.9% and 120.8%, respectively. This suggests that these fibre meshes not only support cell viability but may also enhance cell proliferation, suggesting that they could be suitable for applications in tissue engineering and regenerative medicine, where maintaining cell viability and promoting proliferation are critical. Regarding the 2.5%, 5% and 10% they exhibited excellent cytocompatibility with 95.6%, 98.5% and 98.5% respectively. When comparing the meshes we can identify that there are statistical significant differences as shown in *Table 4.3.5*.

Table 4.3.5: Statistically significant differences in the 72C group against control.

Meshes	(*) for Significance	Interpretation
1% added CNDs to 2.5% added CNDs	*	$p < 0.05$: statistically significant.
0% added CNDs to 1% added CNDs	**	$p < 0.01$: very significant.
Positive control to 2.5% added CNDs	****	$p < 0.0001$: extremely significant.
1% added CNDs to 2.5% added CNDs	****	$p < 0.0001$: extremely significant.
1% added CNDs to 5% added CNDs	****	$p < 0.0001$: extremely significant.
1% added CNDs to 10% added CNDs	****	$p < 0.0001$: extremely significant.

To gain a deeper understanding of the results from the MTT Assay, it is important to note that the groups with a 24-hour incubation period consistently performed worse than their 72-hour counterparts. Empirically, the L929 cell line required approximately 48 hours to achieve 80-90% confluence in the wells, rather than the expected 24 hours, during both the passage and seeding processes. This longer proliferation time could be a key factor contributing to the more biocompatible performances observed in the 72-hour incubation groups.

Additionally, the 24C group, which was tested with freshly incubated media following a media change, was compared to the 72D group, which underwent testing without a media change. This comparison aimed to identify any residual solvents (such as chloroform) or other superficial cytotoxic agents that might have been eliminated through the media change. Despite this, the 72D group still demonstrated better performance than the 24C group with the media change.

The 24C group exhibited the poorest performance among all groups, which may be attributed to potential temperature fluctuations or errors during the aspiration process. Since the media must be removed from the incubator for aspiration and replacement, these factors could have negatively impacted the cell viability.

The 72C group demonstrated the highest performance among all groups, even surpassing the positive control group in terms of cell proliferation. These results suggest that a pre-treatment protocol may be the most effective approach to eliminate any residual solvents prior to potential clinical applications.

Chapter 5

Conclusions and Future Work

5.1 Conclusions

From the results presented in this thesis, the following conclusions can be drawn:

1. The synthesis of CNDs was realised using a one-pot solvothermal method and the obtained percentage yield was of 61.6%.
2. Electropinnability of the polymer PHB was greatly influenced in the concentration, being 10% of PHB the ideal concentration for consistent fibres in single needle and for the core solution of the coaxial electrospinning. This concentration needed to be kept warm (above 40ºC), to be able to electrospin the solution.
3. In coaxial electrospinning, in the fabrication of the shell solution (the one that contains the different concentrations of CNDs), the solution had to be produced with a smaller percentage of polymer than the core solution in order to obtain a homogeneous spread of CNDs in the fibres.
4. The use of the rotating drum collector allowed a better alignment of the fibres because of the tension generated by this type of collector.
5. The fibre diameters obtained in single needle and coaxial electrospinning were highly correlated with the polymer´s electrospinning characteristics of making thicker fibres than other heavily commercialised polymers such as polyacrylonitrile (PAN) under the same electrospinning conditions.
6. The CNDs morphology showed a turbostratic carbon structure under the TEM microscope. Under the TEM and SEM microscopes the different concentration of the fibres showed a similar fibre diameter being the thickest diameter size the single needle electrospinning PHB fibres and the thinnest fibres, the coaxial fibre meshes with 10% added CNDs.
7. EDXS maps revealed the presence of nitrogen in the meshes containing CNDs, with a gradual increase in volume corresponding to higher concentrations.

8. The average hydrodynamic particle size was determined using DLS analysis and was 57.76 nm in volume with a standard deviation of 26.27 nm, showing a unimodal distribution.
9. The ATR-FTIR Spectra showed the characteristic peaks of the different fibre meshes and the CNDs. Unfortunately, it was not possible to determine the addition of CNDs into the different fibre meshes as it was not detectable by the ATR-FTIR equipment.
10. The UV-Vis Absorption Spectrum of the CNDs displayed a bimodal distribution at with absorption peaks at 230 nm and 316 nm. The peak at 230 nm is likely due to π-π^* transitions in the aromatic naphthalene ring and the peak at 316 nm could reflect interactions between the naphthalene and citric acid components in the CNDs, indicating extended conjugation or specific interactions.
11. Fluorescence Spectrum of the CNDs showed a trimodal distribution with emission peaks at 300.2 nm, 332.2 nm and 599.5 nm. The first peak is most likely related to Rayleigh scattering. The second peak at 332.2 nm is potentially because of a return from the excited state of the aromatic system in 1,5-DAN to its ground state, and, finally, the last peak might be due to factors such as extended conjugation in the molecule or interactions with other components in the solution.
12. All the PHB fibre meshes exhibited contact angles greater than 90° signifying a hydrophobic behaviour, except for the coaxial PHB mesh containing 1% CNDs, which showed hydrophilic characteristics. In contrast, the synthesised CNDs had a contact angle near 0°, indicating ideal wetting or spreading.
13. The thermal degradation of the PHB fibre meshes in a nitrogen atmosphere occurs above 230 °C and as a higher concentration of CNDs, a higher temperature is needed to reach the onset temperature and start the degradation process. In the case of the synthetised CNDs, it displayed two degradation curves, with the first one at around 90ºC, most likely the elimination of residual water, and the second one is where the degradation begins at around 400ºC.
14. The PHB fibre meshes melt at around 181-184°C suggesting that the polymer is likely semi-crystalline, as amorphous polymers do not have a defined melting point. Semi-crystalline polymers typically exhibit both crystalline and amorphous regions, resulting in a melting temperature where the crystalline portions transition to a liquid state. Additionally, observing the % crystallised we can see that the fibres as well as the CNDs are semi-crystalline, furthermore justifying that the carbon nanodots have

a turbostratic carbon structure.

15. Regarding the DSC analysis, the PHB fibre meshes melted at around 181-184°C suggesting that the polymer is semi-crystalline. Furthermore, if we observe the % crystallised we can see that CNDs are also semi-crystalline, furthermore justifying that the carbon nanodots have a turbostratic carbon structure.
16. The XPS analysis over the coaxial fibres with the addition of 2.5% and 10% CNDs when compared to the single needle fibres (without addition of CNDs) and the synthesised CNDs, showed the presence of nitrogen in them. Additionally, as the concentration increases so does the percentage of nitrogen in the fibre mesh, signifying that there is an incorporation of the CNDs on the shell layer of the coaxial fibres.
17. Regarding, the MTT Assay results, among all groups, the 72C group achieved the highest level of performance, surpassing even the positive control group regarding cell proliferation. This suggest that a pre-treatment may be the most effective approach for potential clinical applications.

5.1.1 Future work

Because of the one-year duration limit of this project, not all of the possible experiments and characterisation techniques could be performed. Future work that should complement the results of this thesis are:

1) While the fibres synthetised on this thesis were functional and thin, they are at the micrometre size. Further experiments and modification on the selected parameters could perfect the electrospinning process to create fibres on the nanometre range.
2) One of the key future experiments that would be valuable to conduct is antibacterial assays. It would be beneficial to conduct these assays using at least one gram-positive bacterial strain and one gram-negative bacterial strain for comparison. The different concentrations of added CNDs would be evaluated and decided which would be most advantageous for a hernia repair application.
3) Liberation and ROS assays would add much information regarding the nature of the CNDs and how they would perform in a hernia repair application.
4) Due to time constraints, the light activated properties of the CNDs, both individually and within the fibre mesh, were not thoroughly tested. Conducting a ROS Assay and a mechanistic study would be crucial future experiments to evaluate the effectiveness

of light activation for targeted bacterial elimination. Although, a hypothesis exists suggesting how these CNDs, when irradiated with light, generate ROS on command [8]. As the CNDs where synthesised according to the method described in [70], it has been reported that these carbon nanodots produce ROS under light exposure, making them effective for Antimicrobial Photodynamic Inactivation (aPDI). This process integrates a non-toxic photosensitiser (PS), safe visible light and oxygen molecules. aPDI operates via two mechanisms: the Type I mechanism generates ROS such as hydroxyl radicals, superoxide, or hydrogen peroxide, while the Type II mechanism produces singlet oxygen ($^1O_2$). Research indicates that with these synthesised carbon nanodots, the process predominantly relies on the Type II mechanism involving singlet oxygen. These highly reactive species inflict extensive, non-specific damage to pathogens, including bacteria, viruses, parasites and fungi, making aPDI effective aggainst both drug-sensitive and drug-resistant microbes, with minimal risk of resistance development, as previously mentioned in *Subsection 2.3.3*.

5) Using an electrospinning chamber with standardised ambient conditions would enable more reproducible electrospinning processes, and therefore, more coherent results.
6) The time limitation did not allow more useful characterisation techniques that could have elevated this work such as XRD analysis, mechanical testing and RAMAN Spectroscopy. As well, as doing more repetitions of certain characterisation techniques would perfect this work; these techniques being TGA, DSC and XPS analysis.
7) To be able to understand why the PHB fibre meshes with 1% of added CNDs displayed hydrophilic behaviour, more electrospinning experiments at this concentration should be done with variations in the environment to see if this is what is affecting the result.
8) To repeat the MTT Assay would be ideal, to analyse recurring results in order to draw a conclusion that more accurately reflects reality.
9) It would be highly suitable to realise an AlamarBlue™ Assay after the MTT Assay. It would aid to allow determining real-time monitoring of cell health, how well the cells survive and proliferate when they are exposed to the different fibre meshes.

References

[1] Q. Saiding *et al.*, "Abdominal wall hernia repair: from prosthetic meshes to smart materials," Aug. 01, 2023, *Elsevier B.V.* doi: 10.1016/j.mtbio.2023.100691.

[2] Sigma-Aldrich, "SYRINGE NEEDLE CONVERSION SIZE CHART," 2021.

[3] A. L. Komorowski, "History of the Inguinal Hernia Repair," in *Inguinal Hernia*, 2014. doi: 10.5772/58533.

[4] R. C. Read, "Milestones in the history of hernia surgery: Prosthetic repair," *Hernia*, vol. 8, no. 1, pp. 8–14, Feb. 2004, doi: 10.1007/s10029-003-0169-2.

[5] I. Wu and J. Elisseeff, "Biomaterials and Tissue Engineering for Soft Tissue Reconstruction," *Natural and Synthetic Biomedical Polymers*, pp. 235–241, Jan. 2014, doi: 10.1016/B978-0-12-396983-5.00015-6.

[6] Q. Saiding *et al.*, "Abdominal wall hernia repair: from prosthetic meshes to smart materials," Aug. 01, 2023, *Elsevier B.V.* doi: 10.1016/j.mtbio.2023.100691.

[7] C. Wang See, T. Kim, and D. Zhu, "Hernia Mesh and Hernia Repair: A Review," *Engineered Regeneration*, vol. 1, 2020, doi: 10.1016/j.engreg.2020.05.002.

[8] X. Nie *et al.*, "Carbon quantum dots: A bright future as photosensitizers for in vitro antibacterial photodynamic inactivation," *J Photochem Photobiol B*, vol. 206, May 2020, doi: 10.1016/j.jphotobiol.2020.111864.

[9] Radiology Key, "Hernias and Abdominal Wall Pathology." Accessed: Jul. 02, 2024. [Online]. Available: https://radiologykey.com/hernias-and-abdominal-wall-pathology/

[10] NHS, "Hernia," NHS UK. Accessed: Jul. 03, 2024. [Online]. Available: https://www.nhs.uk/conditions/hernia/

[11] John Hopkins Medicine, "Ventral (Abdominal) Hernia," Health. Accessed: Sep. 12, 2024. [Online]. Available: https://www.hopkinsmedicine.org/health/conditions-and-diseases/hernias/ventral-abdominal-hernia#:~:text=What%20is%20a%20ventral%20hernia,specific%20types%20of%20ventral%20hernias.

[12] E. Wales and S. Holloway, "The use of prosthetic mesh for abdominal wall repairs: A semi-systematic-literature review," *Int Wound J*, vol. 16, no. 1, pp. 30–40, Feb. 2019, doi: 10.1111/iwj.12977.

[13] A. Rankin, M. Kostusiak, and A. Sokker, "Spigelian hernia: Case series and review of the literature," *Visc Med*, vol. 35, no. 2, 2019, doi: 10.1159/000494280.

[14] A. Kingsnorth and K. LeBlanc, "Hernias: inguinal and incisional," *The Lancet*, vol. 362, no. 9395, pp. 1561–1571, Nov. 2003, doi: 10.1016/S0140-6736(03)14746-0.

[15] F. Schier and J. Klizaite, "Rare inguinal hernia forms in children," *Pediatr Surg Int*, vol. 20, no. 10, pp. 748–752, Oct. 2004, doi: 10.1007/s00383-004-1291-7.

[16] Royal College of Surgeons of England, "Surgery and the NHS in numbers," Royal College of Surgeons of England. Accessed: Mar. 14, 2024. [Online]. Available: https://www.rcseng.ac.uk/news-and-events/media-centre/media-background-briefings-and-statistics/surgery-and-the-nhs-in-numbers/

[17] National Institute of Health and Care Excellence, "Laparoscopic surgery for inguinal hernia repair," Technology appraisal guidance. Accessed: Sep. 21, 2024. [Online]. Available: https://www.nice.org.uk/guidance/ta83/chapter/implications-for-the-nhs

[18] D. A. Shankar, K. M. F. Itani, W. J. O'Brien, and V. M. Sanchez, "Factors Associated With Long-term Outcomes of Umbilical Hernia Repair," *JAMA Surg*, vol. 152, no. 5, p. 461, May 2017, doi: 10.1001/jamasurg.2016.5052.

[19] N. Chihara *et al.*, "Laparoscopic Repair Using Self-Fixating Mesh in an Adult Patient with a Sciatic Hernia and Irreducible Small Bowel: A Case Report and Literature Review," *Journal of Nippon Medical School*, vol. 90, no. 3, 2023, doi: 10.1272/jnms.JNMS.2023_90-403.

[20] M. Morimoto *et al.*, "Internal supravesical hernia repaired via the anterior approach alone: A case report," *Int J Surg Case Rep*, vol. 39, pp. 297–300, 2017, doi: 10.1016/j.ijscr.2017.08.023.

[21] C. K. Major, M. Aziz, and J. Collins, "Obturator hernia: a case report," *J Med Case Rep*, vol. 15, no. 1, 2021, doi: 10.1186/s13256-021-02793-7.

[22] A. Bedayat *et al.*, "Abdominal wall and pelvic hernias: classic and unusual hernias and their mimics," Aug. 01, 2020, *Elsevier Inc.* doi: 10.1016/j.clinimag.2020.03.007.

[23] A. Svenningsson and T. Wester, "Hernias," in *Pediatric Surgery: Diagnosis and Management*, 2023. doi: 10.1007/978-3-030-81488-5_74.

[24] M. Hammoud and J. Gerken, "Inguinal Hernia," National Center for Biotechnology Information. Accessed: Sep. 21, 2024. [Online]. Available: https://www.ncbi.nlm.nih.gov/books/NBK513332/#article-23527.s5

[25] Z. Morrison, S. Kashyap, and V. L. Nirujogi, "Adult Inguinal Hernia," National Library of Medicine. Accessed: Aug. 05, 2024. [Online]. Available: https://www.ncbi.nlm.nih.gov/books/NBK537241/#:~:text=The%20congenital%20type%20is%20related,lateral%20to%20the%20epigastric%20vessels.

[26] Z. Cooper and S. J. Ferzoco, "Hernias," *Encyclopedia of Gastroenterology*, pp. 379–381, Jan. 2004, doi: 10.1016/B0-12-386860-2/00369-5.

[27] John Hopkins Medicine, "Umbilical Hernia," John Hopkins Medicine. Accessed: Apr. 25, 2024. [Online]. Available: https://www.hopkinsmedicine.org/health/conditions-and-diseases/hernias/umbilical-hernia#:~:text=After%20birth%2C%20the%20umbilical%20cord,muscles%20and%20cause%20a%20hernia.

[28] Z. U. Khan and N. Ahmed, "Anatomy, embryology and pathophysiology of Inguinal Hernia and current trends in Inguinal Hernia treatment," *Pak J Surg*, vol. 37, no. 4, 2021.

[29] S. Prasanna, P. G. Sekaran, A. Sivakumar, and V. K. Govindan, "Role of Collagen in the Etiology of Inguinal Hernia Patients: A Case-Control Study," *Cureus*, Aug. 2023, doi: 10.7759/cureus.43479.

[30] M. G. Kenny, S. Agrawal, C. Crigler, and R. J. Fitzgibbons, "A molecular perspective of obesity-mediated incisional hernia," *Health Sciences Review*, vol. 6, 2023, doi: 10.1016/j.hsr.2023.100080.

[31] D. McDonnell and C. Wakefield, "Adult groin hernias: acute and elective," *Surgery (Oxford)*, vol. 36, no. 5, pp. 238–244, May 2018, doi: 10.1016/J.MPSUR.2018.03.003.

[32] Y. Li *et al.*, "Advances, challenges, and prospects for surgical suture materials," 2023. doi: 10.1016/j.actbio.2023.07.041.

[33] W. Liu, Y. Xie, Y. Zheng, W. He, K. Qiao, and H. Meng, "Regulatory science for hernia mesh: Current status and future perspectives," *Bioact Mater*, vol. 6, no. 2, 2021, doi: 10.1016/j.bioactmat.2020.08.021.

[34] A. Keirouz *et al.*, "The History of Electrospinning: Past, Present, and Future Developments," Jun. 09, 2023, *John Wiley and Sons Inc.* doi: 10.1002/admt.202201723.

[35] F. J. Davis, S. D. Mohan, and M. A. Ibraheem, "Chapter 1. Introduction," 2015, pp. 1–21. doi: 10.1039/9781849735575-00001.

[36] H. J. Kull, "Theory of the Rayleigh-Taylor instability," *Phys Rep*, vol. 206, no. 5, pp. 197–325, Aug. 1991, doi: 10.1016/0370-1573(91)90153-D.

[37] M. Z. A. Zulkifli, D. Nordin, N. Shaari, and S. K. Kamarudin, "Overview of Electrospinning for Tissue Engineering Applications," 2023. doi: 10.3390/polym15112418.

[38] J. Zeleny, "Instability of Electrified Liquid Surfaces," *Physical Review*, vol. 10, no. 1, pp. 1–6, Jul. 1917, doi: 10.1103/PhysRev.10.1.

[39] M. G. M. C. Mori da Cunha *et al.*, "Functional supramolecular bioactivated electrospun mesh improves tissue ingrowth in experimental abdominal wall reconstruction in rats," *Acta Biomater*, vol. 106, pp. 82–91, Apr. 2020, doi: 10.1016/j.actbio.2020.01.041.

[40] K. Zhang and L. Zhu, "Transversalis fascia suture reinforcement may facilitate the performance of electrospun P(LLA-CL) nanoscale fibrinogen mesh in inguinal hernia repair: a prospective single-center cohort study," *Sci Rep*, vol. 13, no. 1, Dec. 2023, doi: 10.1038/s41598-023-39391-0.

[41] R. Rynkevic *et al.*, "In vitro simulation of in vivo degradation and cyclic loading of novel degradable electrospun meshes for prolapse repair," *Polym Test*, vol. 78, 2019, doi: 10.1016/j.polymertesting.2019.105957.

[42] L. Hympanova *et al.*, "Experimental reconstruction of an abdominal wall defect with electrospun polycaprolactone-ureidopyrimidinone mesh conserves compliance yet may have insufficient strength," *J Mech Behav Biomed Mater*, vol. 88, 2018, doi: 10.1016/j.jmbbm.2018.08.026.

[43] G. F. El Fawal, "Polymer Nanofibers Electrospinning: A review," 2020. doi: 10.21608/ejchem.2019.14837.1898.

[44] T. Zhang *et al.*, "Bioinspired Platelet-Anchored Electrospun Meshes for Tight Inflammation Manipulation and Chronic Diabetic Wound Healing," *Macromol Biosci*, vol. 23, no. 10, 2023, doi: 10.1002/mabi.202300036.

[45] I. J. Hall Barrientos *et al.*, "Fabrication and characterisation of drug-loaded electrospun polymeric nanofibers for controlled release in hernia repair," *Int J Pharm*, vol. 517, no. 1–2, 2017, doi: 10.1016/j.ijpharm.2016.12.022.

[46] V. Kundrat, N. Cernekova, A. Kovalcik, V. Enev, and I. Marova, "Drug release kinetics of electrospun PHB meshes," *Materials*, vol. 12, no. 12, Jun. 2019, doi: 10.3390/ma12121924.

[47] M. Adnan *et al.*, "Polyhydroxybutyrate (PHB)-Based Biodegradable Polymer from Agromyces indicus: Enhanced Production, Characterization, and Optimization," *Polymers (Basel)*, vol. 14, no. 19, Oct. 2022, doi: 10.3390/polym14193982.

[48] M. Kervran, C. Vagner, M. Cochez, M. Ponçot, M. R. Saeb, and H. Vahabi, "Thermal degradation of polylactic acid (PLA)/polyhydroxybutyrate (PHB) blends: A systematic review," Jul. 01, 2022, *Elsevier Ltd.* doi: 10.1016/j.polymdegradstab.2022.109995.

[49] World Health Organization, "CONSTITUTION OF THE WORLD HEALTH ORGANIZATION." Accessed: Aug. 30, 2024. [Online]. Available: https://apps.who.int/gb/bd/pdf/bd47/en/constitution-en.pdf

[50] M. Ruggeri *et al.*, "Nanotechnology-based medical devices for the treatment of chronic skin lesions: From research to the clinic," *Pharmaceutics*, vol. 12, no. 9, 2020, doi: 10.3390/pharmaceutics12090815.

[51] A. Haleem, M. Javaid, R. P. Singh, S. Rab, and R. Suman, "Applications of nanotechnology in medical field: a brief review," *Global Health Journal*, vol. 7, no. 2, 2023, doi: 10.1016/j.glohj.2023.02.008.

[52] N. T. Kalyani and S. J. Dhoble, "Introduction to nano materials," *Quantum Dots: Emerging Materials for Versatile Applications*, pp. 3–40, Jan. 2023, doi: 10.1016/B978-0-323-85278-4.00010-6.

[53] H. Manisha, P. D. Priya Swetha, Y. B. Shim, and K. S. Prasad, "Revisiting fluorescent carbon nanodots for environmental, biomedical applications and puzzle about fluorophore impurities," Oct. 01, 2019, *Elsevier B.V.* doi: 10.1016/j.nanoso.2019.100391.

[54] K. A. Altammar, "A review on nanoparticles: characteristics, synthesis, applications, and challenges," 2023, *Frontiers Media S.A.* doi: 10.3389/fmicb.2023.1155622.

[55] S. N. Alam *et al.*, “An introduction to triboelectric nanogenerators,” *Nano-Structures & Nano-Objects*, vol. 34, p. 100980, Apr. 2023, doi: 10.1016/J.NANOSO.2023.100980.

[56] D. Bhartiya, A. Awasthi, and D. Marla, “Synthesis methods of nanotubes,” *Graphene, Nanotubes and Quantum Dots-Based Nanotechnology: Fundamentals and Applications*, pp. 251–280, Jan. 2022, doi: 10.1016/B978-0-323-85457-3.00018-9.

[57] J. Zhang, W. Tang, X. Zhang, Z. Song, and T. Tong, “An Overview of Stimuli-Responsive Intelligent Antibacterial Nanomaterials,” 2023. doi: 10.3390/pharmaceutics15082113.

[58] S. Kohno *et al.*, “Analysis of risk factors for surgical site infection and postoperative recurrence following inguinal and femoral hernia surgery in adults,” *Asian J Surg*, vol. 45, no. 4, pp. 1001–1006, Apr. 2022, doi: 10.1016/j.asjsur.2021.08.019.

[59] J. J. Kanitra, A. L. Hess, P. S. Haan, C. I. Anderson, and S. Kavuturu, “Hernia recurrence and infection rate in elective complex abdominal wall repair using biologic mesh,” *BMC Surg*, vol. 19, no. 1, Nov. 2019, doi: 10.1186/s12893-019-0640-3.

[60] R. Knoblauch *et al.*, “Antimicrobial carbon nanodots: Photodynamic inactivation and dark antimicrobial effects on bacteria by brominated carbon nanodots,” *Nanoscale*, vol. 13, no. 1, pp. 85–99, Jan. 2021, doi: 10.1039/d0nr06842j.

[61] J. F. Han *et al.*, “Chemiluminescent carbon nanodots for dynamic and guided antibacteria,” *Light Sci Appl*, vol. 12, no. 1, Dec. 2023, doi: 10.1038/s41377-023-01149-8.

[62] L. Hochvaldová *et al.*, “Antibacterial nanomaterials: Upcoming hope to overcome antibiotic resistance crisis,” 2022. doi: 10.1515/ntrev-2022-0059.

[63] M. Xie *et al.*, “Antibacterial Nanomaterials: Mechanisms, Impacts on Antimicrobial Resistance and Design Principles,” 2023. doi: 10.1002/anie.202217345.

[64] X. Miao *et al.*, “Synthesis of Carbon Dots with Multiple Color Emission by Controlled Graphitization and Surface Functionalization,” *Advanced Materials*, vol. 30, no. 1, Jan. 2018, doi: 10.1002/adma.201704740.

[65] “56. Rapid synthesis of multifunctional carbon nanodots as effective antioxidants and antibacterial agent”.

[66] Y. Chai, Y. Feng, K. Zhang, and J. Li, “Preparation of Fluorescent Carbon Dots Composites and Their Potential Applications in Biomedicine and Drug Delivery—A Review,” Nov. 01, 2022, *MDPI*. doi: 10.3390/pharmaceutics14112482.

[67] F. Yuan *et al.*, “Bright Multicolor Bandgap Fluorescent Carbon Quantum Dots for Electroluminescent Light-Emitting Diodes,” *Advanced Materials*, vol. 29, no. 3, Jan. 2017, doi: 10.1002/adma.201604436.

[68] M. R. Hamblin, “Antimicrobial photodynamic inactivation: a bright new technique to kill resistant microbes,” *Curr Opin Microbiol*, vol. 33, pp. 67–73, Oct. 2016, doi: 10.1016/J.MIB.2016.06.008.

[69] Q. Xin *et al.*, “Antibacterial Carbon-Based Nanomaterials,” *Advanced Materials*, vol. 31, no. 45, 2019, doi: 10.1002/adma.201804838.

[70] X. Nie *et al.*, “Carbon quantum dots: A bright future as photosensitizers for in vitro antibacterial photodynamic inactivation,” *J Photochem Photobiol B*, vol. 206, May 2020, doi: 10.1016/j.jphotobiol.2020.111864.

[71] abcam, “MTT Assay Kit (Cell Proliferation) ab211091,” abcam. Accessed: May 02, 2024. [Online]. Available: https://www.abcam.com/en-us/products/assay-kits/mtt-assay-kit-cell-proliferation-ab211091

[72] G. K. Srivastava *et al.*, “Comparison between direct contact and extract exposure methods for PFO cytotoxicity evaluation,” *Sci Rep*, vol. 8, no. 1, Dec. 2018, doi: 10.1038/s41598-018-19428-5.

[73] International Organization for Standardization, “Biological evaluation of medical devices- Part 5: Tests for in vitro cytotoxicity. ISO 10993-5:2009(E),” Switzerland,

2009. Accessed: Apr. 26, 2024. [Online]. Available: https://nhiso.com/wp-content/uploads/2018/05/ISO-10993-5-2009.pdf

[74] Z. X. Huang, J. W. Wu, S. C. Wong, J. P. Qu, and T. S. Srivatsan, "The technique of electrospinning for manufacturing core-shell nanofibers," Jan. 25, 2018, *Taylor and Francis Inc.* doi: 10.1080/10426914.2017.1303144.

[75] C. Bommier, D. Mitlin, and X. Ji, "Internal structure – Na storage mechanisms – Electrochemical performance relations in carbons," *Prog Mater Sci*, vol. 97, pp. 170–203, Aug. 2018, doi: 10.1016/J.PMATSCI.2018.04.006.

[76] P. Ruz, S. Banerjee, M. Pandey, V. Sudarsan, P. U. Sastry, and R. J. Kshirsagar, "Structural evolution of turbostratic carbon: Implications in H2 storage," *Solid State Sci*, vol. 62, pp. 105–111, Dec. 2016, doi: 10.1016/J.SOLIDSTATESCIENCES.2016.10.017.

[77] L. Xiao and H. Sun, "Novel properties and applications of carbon nanodots," Nov. 01, 2018, *Royal Society of Chemistry*. doi: 10.1039/c8nh00106e.

[78] V. Guerrero-Florez, A. Barbara, S. Kodjikian, F. Oukacine, P. Trens, and X. Cattoën, "Dynamic light scattering unveils stochastic degradation in large-pore mesoporous silica nanoparticles," *J Colloid Interface Sci*, vol. 676, pp. 1098–1108, Dec. 2024, doi: 10.1016/J.JCIS.2024.07.151.

[79] D. L. Pavia, G. M. Lampman, and G. S. Kriz, *Introduction to Spectroscopy. A guide for students of Organic Chemistry*, Third edition. ThomsonLearning, 2001.

[80] P. Atkins and J. de Paula, *Elements of Physical Chemistry*, Fifth Edition. New York: Oxford Publisher Press Inc, 1992.

[81] G. Giridhar, R. K. N. R. Manepalli, and G. Apparao, "Contact Angle Measurement Techniques for Nanomaterials," *Thermal and Rheological Measurement Techniques for Nanomaterials Characterization*, vol. 3, pp. 173–195, Jan. 2017, doi: 10.1016/B978-0-323-46139-9.00008-6.

[82] J. D. Menczel, L. Judovits, R. B. Prime, H. E. Bair, M. Reading, and S. Swier, "Differential Scanning Calorimetry (DSC)," in *Thermal Analysis of Polymers*, Wiley, 2009, pp. 7–239. doi: 10.1002/9780470423837.ch2.

[83] M. Smith, L. Scudiero, J. Espinal, J. S. McEwen, and M. Garcia-Perez, "Improving the deconvolution and interpretation of XPS spectra from chars by ab initio calculations," *Carbon N Y*, vol. 110, pp. 155–171, Dec. 2016, doi: 10.1016/J.CARBON.2016.09.012.

[84] M. Ayiania, M. Smith, A. J. R. Hensley, L. Scudiero, J. S. McEwen, and M. Garcia-Perez, "Deconvoluting the XPS spectra for nitrogen-doped chars: An analysis from first principles," *Carbon N Y*, vol. 162, pp. 528–544, Jun. 2020, doi: 10.1016/J.CARBON.2020.02.065.

Appendix

This work was presented as a flash poster at the BioMedEng 2024 conference in London, UK, under the title of *Light Activated Antibacterial Membranes for Hernia Repair*. The conference took place on the 5th and 6th of September, 2024.